APPLIED SCIENCES AND ENGINEERING

Conformability of flexible sheets on spherical surfaces

Siyi Liu[1]*, Jinlong He[2]*, Yifan Rao[1], Zhaohe Dai[3], Huilin Ye[4], John C. Tanir[1], Ying Li[2]*, Nanshu Lu[1,5]*

Three-dimensional surface-conformable electronics is a burgeoning technology with potential applications in curved displays, bioelectronics, and biomimetics. Flexible electronics are notoriously difficult to fully conform to nondevelopable surfaces such as spheres. Although stretchable electronics can well conform to nondevelopable surfaces, they need to sacrifice pixel density for stretchability. Various empirical designs have been explored to improve the conformability of flexible electronics on spherical surfaces. However, no rational design guidelines exist. This study uses a combination of experimental, analytical, and numerical approaches to systematically investigate the conformability of both intact and partially cut circular sheets on spherical surfaces. Through the analysis of thin film buckling on curved surfaces, we identify a scaling law that predicts the conformability of flexible sheets on spherical surfaces. We also quantify the effects of radial slits on enhancing conformability and provide a practical guideline for using these slits to improve conformability from 40% to more than 90%.

INTRODUCTION

Thin-film electronics can simultaneously benefit from well-established wafer-based electronics manufacturing processes and unconventional mechanical deformability. For example, flexible displays that can curve and fold have been successfully industrialized as curved or even rollable computer monitors, televisions, and cellphone screens. However, today's flexible displays are only able to form or conform to developable surfaces that have zero Gaussian curvatures and can fully unroll onto a plane. Thin-film electronics able to conform to three-dimensional (3D) curvilinear surfaces (*1*) can unleash much broader possibilities, particularly body-conformable electronics (*2*), surface-conformable antenna (*3*), conformal electronic armor (*4*), bioinspired electronic eyes (*5*, *6*), and so on. Well-known examples of body-conformable electronics include epidermal electronics intimately but noninvasively coupled to the skin (*7*), ultrathin electrocorticography (ECoG) electrodes accommodating brain curvature and movement (*8*), e-dura surrounding the spinal cord (*9*), glucose-sensing contact lenses (*10*) or artificial retina with a matching curvature to the eyeball (*11*), etc. Achieving an intimate but nonirritating contact between electronics and living tissue surfaces is crucial for tissue health, high-fidelity sensing, and the mechanical durability of the device (*12*, *13*), but it is challenging because of the intrinsic geometric mismatch between as-fabricated planar electronics and naturally curved tissue surfaces.

When the target surface is nondevelopable (i.e., with nonzero Gaussian curvatures, e.g., spherical surface), Gauss's *Theorema Egregium* indicates that stretching or compression of the thin-film electronics is required (*14*). In the past, tremendous efforts have been exerted on material design and structural engineering to improve the stretchability of thin-film devices (*15*, *16*). On the one hand, intrinsically soft and stretchable materials, including organic materials, liquid-phase materials, hydrogels, and nanocomposites, have been created and widely applied in body-conformable electronics (*17*–*19*). On the other hand, various stretchable structures have been proposed to achieve body conformability, including mesh design (*20*), kirigami design (*21*, *22*), serpentine structures (*7*), and buckled structures (*23*). However, state-of-the-art stretchable electronics are not entirely adequate for body-conformable electronics for the following two reasons. First, there is a well-known trade-off between device stretchability and performance, such as low conductivity or mobility in intrinsically soft electronic materials (*2*, *24*) or low areal coverage of active devices due to the real estate consumed by the stretchable interconnects such as serpentines (*2*, *25*). Second, the fabrication of many stretchable electronics is not fully compatible with well-established wafer-based microfabrication processes (*26*), which prevents the incorporation of many high-performance electronic components and limits their industrialization.

When a high-performance electronic sheet is flexible but too stiff to stretch, it has to buckle and delaminate from the underlying nondevelopable substrate to release the compressive strain energy. Several strategies have been proposed to avoid buckling and enhance conformability. Inspired by soccer balls, Choi *et al.* (*11*) demonstrated an empirical truncated icosahedron design with cuts for a high-density (1935 pixels within 3 mm^2), 1.4-μm-thick artificial retina to well conform to an eyeball without any stretchable structures, as shown in Fig. 1A. However, this design is empirical and hard to generalize. In a different design, a planar 1D array of petal-shaped ribbons can perfectly wrap a hemispherical surface that mimics the closure of a bud, as shown in Fig. 1B (*27*), but it is not applicable in high-performance electronics because its limited device integrity requires perfect alignments during the wrapping process. For complicated 3D surfaces, computational methods were built to discretize the target surface into hundreds of small flat elements, which can be deployed into a planar design (*28*). In addition, kirigami designs with optimized small cuts can also morph 2D sheets into deterministic 3D surfaces but with

[1]Center for Mechanics of Solids, Structures and Materials, Department of Aerospace Engineering and Engineering Mechanics, The University of Texas at Austin, TX 78712, USA. [2]Department of Mechanical Engineering, University of Wisconsin-Madison, Madison, WI 53706 - 1572, USA. [3]Department of Mechanics and Engineering Science, College of Engineering, Peking University, Beijing 100871, China. [4]Department of Mechanical Engineering, University of Connecticut, Storrs, CT 06269, USA. [5]Departments of Biomedical Engineering, Electrical and Computer Engineering, and Mechanical Engineering; Texas Materials Institute; and Wireless Networking and Communications Group, The University of Texas at Austin, TX 78712, USA.
*These authors contributed equally to this work.
*Corresponding author. Email: nanshulu@utexas.edu (N.L.); yli2562@wisc.edu (Y.L.)

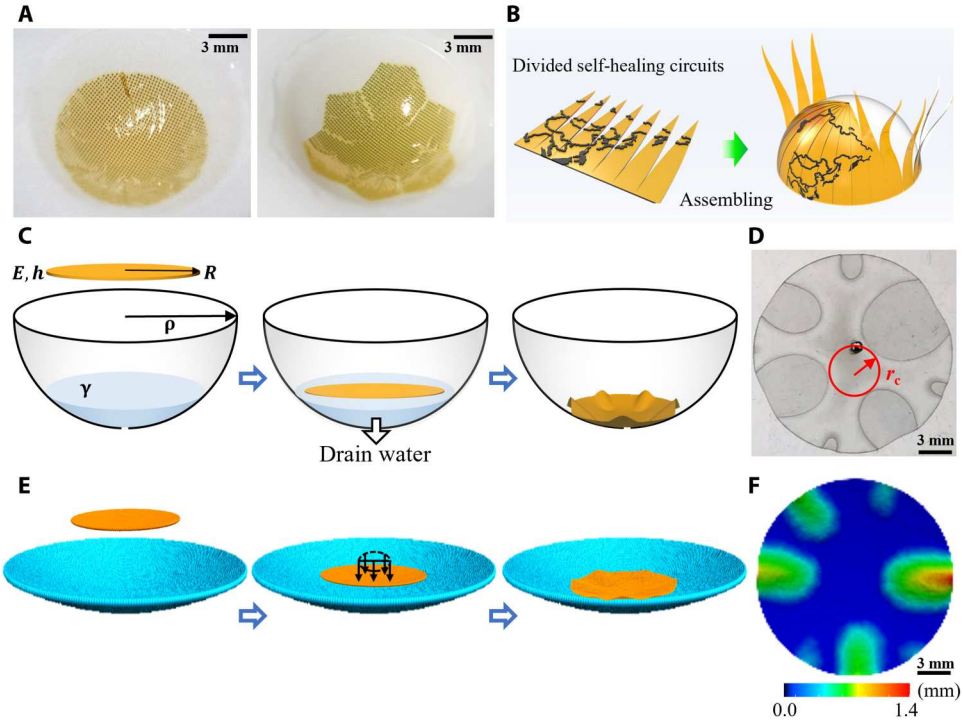

Fig. 1. Research on conforming a flexible sheet to a spherical surface. (**A**) Images of 1.4-μm-thick image sensor arrays with circular design (left) and truncated icosahedron design conformed to a concave spherical poly(dimethylsiloxane) substrate. Reproduced from (*11*) with the permission of Springer Nature. (**B**) Planar array of petal-like ribbons can be perfectly assembled onto a hemispherical surface. Reproduced from (*27*) with the permission of John Wiley and Sons. (**C**) Our experimental setup. Water-assisted transfer of a 13-μm-thick polyethylene terephthalate (PET) sheet of radius R to a rigid hemispherical container with radius ρ: (i) The sheet was placed on water in a hemispherical container with a hole drilled in the bottom. (ii) Water was drained through the hole. (iii) The sheet formed stable conforming pattern after water was drained. (**D**) Top-down optical image of a 9-mm-radius PET sheet conformed to a 30-mm-radius container. r_c is the maximum radius of complete contact. (**E**) Our coarse-grained molecular dynamics (CGMD) simulation setup: (i) A sheet was placed on water in a hemispherical container. (ii) Uniform pressure was applied to the sheet to drive the contact. (iii) The sheet conformed to the spherical container. (**F**) The CGMD result of the gap between the sheet and the spherical surface for R = 9 mm and ρ = 30 mm.

compromised areal coverage (*29*). However, in applications demanding high device densities such as the displays or the artificial retina, too many small elements or cuts disrupt the integrity of the device and hamper self-conformation on the curved surfaces. Hitherto, there lacks a rational but practical guideline to design planar flexible sheets to achieve 3D surface conformability. This prompts us to investigate the buckling-controlled conformability on nondevelopable surfaces for both intact and cut-engineered sheets.

Adhering circular thin sheets to spherical surfaces has been studied for their delamination patterns and the maximum size of complete contact, i.e., the largest radius that can be drawn without intersecting with any buckling zone. Previous studies discovered that there exists a critical radius, below which the sheet can always fully conform to the sphere, but beyond it, buckle delamination starts to appear and different delamination patterns can form depending on the sheet radius (*30*). Although the deformation is nonlinear and the buckling patterns have some stochasticity, the maximum size of complete contact was found to be controlled by the substrate curvature, the interfacial adhesion, and the sheet stiffness but independent of the sheet size, which has been proved theoretically and validated by experiments and molecular dynamics simulations (*30*–*33*). Box *et al.* (*34*) further investigated the number of buckle delaminations of an ultrathin sheet under radial stretching during the conforming process. However, none of the existing theories can capture the area of the delaminated regions, and hence, the overall conformability is not yet predictable.

In this work, we first quantify the overall conformability and the shape of the buckle-delaminated region through experiments and coarse-grained molecular dynamics (CGMD). Next, a scaling relation is derived to describe the shape and number of delaminated regions, which, in reciprocal, yields the conformed region. At the end, we investigate how radial cuts emanating from the edge may enhance the conformability, which leads to a simple yet effective guideline for cut-facilitated conformable designs.

RESULTS

Conforming flexible sheets to spherical surfaces

As many in vivo flexible electronics conform to biotissues with the presence of body fluids (*9*, *11*), plus water-assisted transfer of soft electronics has been widely reported (*35*, *36*), we chose a conforming process through draining dyed water between a circular thin sheet and a hemispherical container with a small hole opened at the bottom, as illustrated by the schematics in Fig. 1C. The thin sheet has a known thickness h, radius R, and Young's modulus E, and the rigid hemispherical bowl has a known radius ρ. The dyed water with a known surface tension γ drives the thin sheet to contact the hemispherical surface during water draining and also offers the

interfacial adhesion after the thin sheet contacts the hemispherical surface. Experimentally, we selected commercially available 13-μm-thick polyethylene terephthalate (PET) to be a good mechanical representative of many flexible electronics (*37*, *38*). The radii of the circular PET sheets varied from 3 to 14 mm in our study. We chose rigid hemispherical surfaces with radii ranging from 30 to 70 mm as good surrogates of human organ geometries such as the heart and the brain. Although biotissues are mechanically soft and geometrically diverse, our current study is limited to rigid spherical surfaces to establish the first viable framework to unravel the conformability of flexible thin sheets to nondevelopable surfaces. Figure 1D offers an experimental top-down view after an intact circular PET sheet of 9-mm radius formed a stable conforming pattern on a rigid hemispherical surface of 30-mm radius. Multiple fingertip-shaped buckle delaminations emanated from the edge of the sheet can be observed, similar to the branched pattern reported by Hure *et al.* (*30*). In Fig. 1D, drawing the largest possible circle without intersecting with any buckle delamination yields the maximum radius of complete contact (*30*–*33*), which is labeled as r_c. Numerically, we performed CGMD to simulate the conforming process as illustrated in Fig. 1E and movie S1. The PET sheet and the rigid hemispherical container were simulated by lattice-spring models (*39*, *40*), and an estimated pressure equivalent to the conforming driving force was applied to the sheet to mimic the water draining process. After the system achieved an equilibrium state, buckle delaminations emerged when R/ρ was large enough. Detailed experimental procedures and CGMD model setup can be found in Materials and Methods.

Figure 2A displays the top-down views of experimental and simulation results for various ratios of R/ρ, based on which we quantified the conformability and plotted them as markers in Fig. 2B. We define conformability to be the fraction of all the sheet areas in contact, i.e.

$$C = \frac{A_{\text{contact}}}{A_{\text{sheet}}} \tag{1}$$

In our study, we limited the PET sheet radius to be $R/\rho < 1/3$, beyond which there could be more than 2% error between the arc length in top-down projected 2D views and that on actual 3D curved surfaces. As there exist multiple equilibrium conforming states for a given configuration, although Fig. 2A only displays one experiment and one simulation result for each R/ρ, at least three independent experiments and five independent simulations were performed for each configuration for us to plot the average values as the markers (solid markers for experiments and open markers for simulations) and the standard deviations as the error bars in Fig. 2B. We can make the following essential observations out of Fig. 2:

1) Despite variations in equilibrium states from one experiment (simulation) to another, reasonably good agreement between experiments and simulation has been achieved in terms of both conforming patterns (Fig. 2A) and conformability (Fig. 2B).

2) Given sheet thickness, modulus, and adhesion, R and ρ control the conformability only through R/ρ, not separately.

3) When R/ρ is below a critical size, 100% conformability can be achieved, which is consistent with existing studies (*30*–*33*).

4) As R/ρ increases, buckle delamination emerges, and conformability declines monotonically.

5) Large and small buckle delaminations may coexist when R/ρ is large (Fig. 2A). Although the simulated number and location of large and small buckle delaminations do not fully agree with experiments, this does not affect the agreement on overall conformability, as evident in Fig. 2B.

The aggregated monotonic relationship between conformability versus R/ρ given in Fig. 2B implies that a scaling law (the black curve) could be found after the physics is revealed. It motivates us to investigate the buckle delamination of thin sheets conforming to curved surfaces to predict the number and shape of buckle delaminations and, ultimately, the overall conformability. However, given the stochastic conforming process, a prediction for the shape of each individual buckle delamination would be impossible. Therefore, the focus of our following analysis is the overall conformability.

Geometric features of blisters

Following the convention of mechanics of buckle delamination (*41*, *42*), we refer buckle delaminations to be blisters from now on. As shown in Fig. 2A, all the blisters extend radially from the edge toward the center of the sheet with fingertip-shaped terminations. If we denote the total number of blisters as N and the edge wavelength and the radial extent of the ith blister as $\lambda_{e,i}$ and $r_{b,i}$, respectively, the total area out of contact can be estimated by the product of the three parameters

$$A_{\text{blister}} \sim \sum_{i=1}^{N} \lambda_{e,i} r_{b,i} \sim N \bar{\lambda}_e \bar{r}_b \tag{2}$$

where $\bar{\lambda}_e$ and $\bar{r}_b$ represent the average edge wavelength and the average radial extent of the N blisters. Among the three unknowns in Eq. 2

$$\bar{r}_b \approx R - r_c \tag{3}$$

where r_c is the radius of the maximum complete contact zone, which has been investigated before and will be discussed later.

Obtaining N and λ_e is a new effort, which requires us to analyze the geometric features of the blisters. For a flat sheet trying to conform to a spherical surface without any external stretching applied, hoop compression emerges in the sheet. When the hoop compressive strain exceeds the critical buckling strain, blisters form to release the hoop strains. As the surface tension of water (72.8 mN/m) is negligible compared to the tensile stiffness (39 kN/m) of the PET sheet, there is no radial strain in the blisters either. According to the *Theorema Egregium* or the compatibility conditions, the parts of blisters far from the delamination fronts should maintain Gaussian curvatures as close to zero as possible, which helps minimize the overall strain energy. As the blisters are curved in the hoop direction, they must have zero curvatures in the other direction, e.g., the radial direction or the axis of symmetry of the blister.

To validate these expectations on the geometric features of blisters, 3D scans using an optical profilometer (Fig. 3A, left) and CGMD simulations (Fig. 3A, right) were performed and compared for two scenarios: R = 5 mm, ρ = 50 mm (Fig. 3) and R = 7 mm, ρ = 50 mm (fig. S1). The sheet deflections along the symmetric axes of the two blisters in Fig. 3A are plotted as dotted lines (blister 1) and dashed lines (blister 2) in Fig. 3B, in which green curves are from experiments and red ones are from simulations. The sheet deflections at no blister region (line 0 in Fig. 3A) are

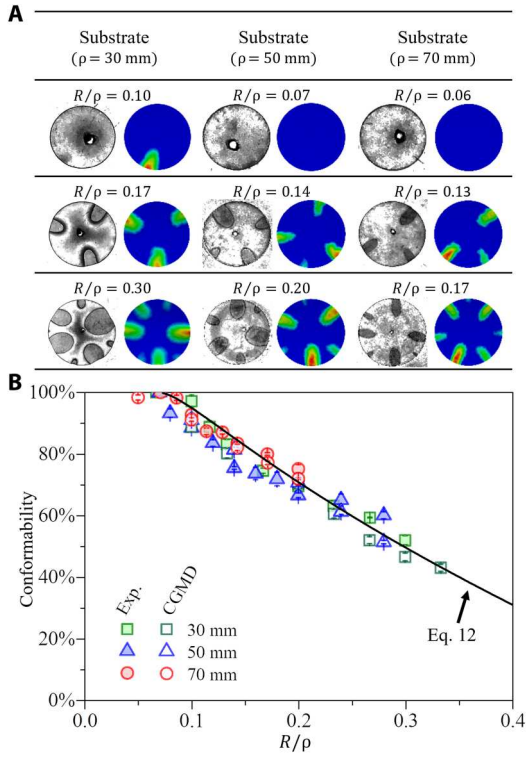

Fig. 2. Experimental and simulated conformability. (**A**) Grayscale optical images (left) and CGMD simulation results (right) for nine different configurations in the top-down views. (**B**) Conformability plotted as a function of normalized sheet radius R/ρ. Solid markers are from experiments, and open markers are from simulations. Error bars represent the standard deviations of multiple trials. The black curve is a scaling law given by Eq. 12.

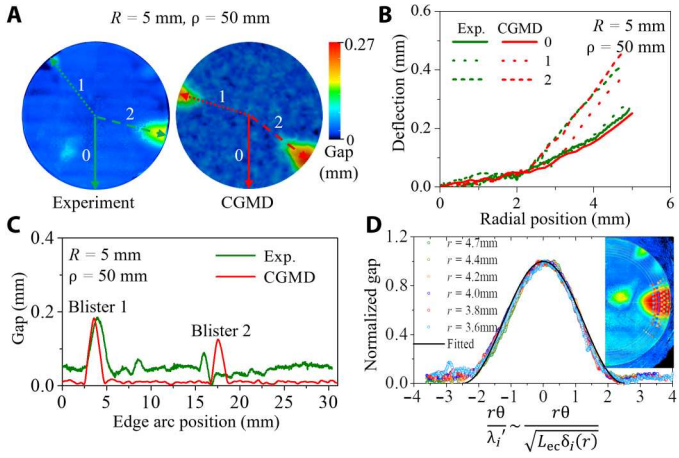

Fig. 3. Geometric features of blisters in the configuration of R = 5 mm and ρ = 50 mm. (**A**) Contour plots of the gap between the sheet and the spherical substrate by experimental 3D scan (left) and CGMD simulation (right). (**B**) Sheet deflection along the radial direction at fully conformed region (solid curves) and the symmetric axes of two blisters (dashed and dotted curves). (**C**) The gap between the sheet and the substrate along the periphery of the circular sheet. (**D**) Normalized hoop profiles at different radial positions of the same blister in an experiment. The black curve corresponds to a sinusoidal shape given by $[1 + \cos(2\pi r\theta/5)]/2$. The inset illustrates the circumferential cuts far from the delamination front to obtain the plotted profiles.

plotted as solid curves in Fig. 3B as references, which are circular arcs. The straight dashed and dotted lines in Fig. 3B indicate that there is zero curvature in the direction for blisters 1 and 2, confirming that the no radial membrane strain argument is true.

The gap between the sheet and the spherical surface along the periphery of the sheet is plotted in Fig. 3C. The wavelength and amplitude of the blister at the edge of the sheet, (λ_e, δ_e), can be measured out of this plot. To confirm that the blister has self-similar hoop cross sections along the radial direction, we plot the normalized hoop blister profiles at different radii far from the delamination front in Fig. 3D. Note that the deflection close to the delamination front does not have the same self-similar profile (*43*). The delaminated gap is normalized by the profile amplitude, δ_i such that all the curves peak at 1. The wavelength is normalized by the estimated wavelength of a corresponding 1D blister based on the buckling amplitude $\lambda_i' \sim \sqrt{L_{ec}\delta_i(r)}$ (*44*), where $L_{ec} = \sqrt{B/\gamma}$ is the elasto-capillary length and B is the flexural rigidity of the sheet, i.e., $B = Eh^3/12(1-\nu^2)$. It is evident in Fig. 3D that after normalization, the cross-sectional profiles at different radii collapse into a single sinusoidal shape, indicating that the amplitude and the wavelength of different hoop cross sections of a blister follow the same scaling law with the same prefactor. Therefore, the crest curvature of a 2D blister formed on a curved surface given by δ/λ^2 is only controlled by the elasto-capillary length L_{ec}. This discovery offers a valuable insight that we can treat such 2D blisters as quasi-1D blisters and use their edge profile (λ_e, δ_e) to fully represent their shapes.

Scaling analysis

If we can derive a scaling law for $A_{blister}$, because $A_{sheet} = A_{contact} + A_{blister}$, then conformability defined in Eq. 1 can be expressed as

$$C = 1 - \frac{A_{blister}}{A_{sheet}} \tag{4}$$

According to Eq. 2, our task is to explore how the blister radial extent r_b, blister edge wavelength λ_e, and the number of blisters N scale with given geometric parameters and material/interface properties.

To obtain r_b, we just need to find out r_c according to Eq. 3. Majidi and Fearing (*31*) first theoretically derived a scaling law for r_c, and Hure *et al.* (*30*) have experimentally validated this scaling law and offered a fitted prefactor

$$r_c = 1.9\rho\left(\frac{\gamma}{Eh}\right)^{1/4} \tag{5}$$

It indicates that the maximum contact radius is proportional to the radius of the spherical surface and independent of the sheet radius. Note that the sheet is not subjected to any radial stretching during our conforming process, so r_c scales with $(\gamma/Eh)^{1/4}$ instead of $(\gamma/Eh)^{1/2}$, which is for sheets under radial stretching (*45*, *46*) In our experiments, the Young's modulus of the PET sheet is E = 3 GPa, the sheet thickness is 13 μm, and the surface tension of water is γ = 72.8 mN/m, so Eq. 5 predicts the maximum contact radius to be r_c = 0.07ρ. For substrates with radii of 30, 50, and 70 mm, Eq. 5 predicts r_c to be 2.1, 3.5, and 4.9 mm, respectively. In our experiments as shown in fig. S2, we find that the maximum sheet radius of complete contact is smaller than 3 mm, falls between 3.5 and 4 mm, and falls

between 5 and 6 mm for the substrate with radii of 30, 50, and 70 mm, respectively. Therefore, our experimental observations of the maximum sheet radius of complete contact are almost consistent with Eq. 5 predictions. To further visualize the linear relationship between r_c and ρ, we plot our experimentally measured r_c (fig. S2) versus ρ in Fig. 4A, which shows that the experimental data scatter around the linear curve. The scatter does not show a correlation with the sheet radius and may be attributed to the initial imperfections of the PET sheet (e.g., preexisting folds or wrinkles). In summary, the existing scaling law for r_c is validated by our experiments.

There is no available scaling law for λ_e, so we have to find it by ourselves. We recall that for a 1D blister on a flat surface, its crest radius of curvature is controlled by the elasto-capillary length (*44*)

$$\frac{\lambda^2}{\delta} \sim L_{ec} \tag{6}$$

For 2D blisters on spherical surfaces, the radius of the substrate ρ can play a role in the bending of the blisters and affect the prefactor of Eq. 6. Hence, we analyze 2D blisters in experiments and simulations to study the effect of substrate radius. For the simulation results, the average edge profiles λ_e and δ_e were extracted out of 10 independent simulations. The range of R/ρ was 0.1 to 0.28 in simulations. In experiments, the λ_e and δ_e of every blister were measured out of the 3D optical profilometer scans (Fig. 3 and fig. S1). For the blisters that we investigated, we plot δ_e as a function of λ_e^2/L_{ec} in Fig. 4B and found a strong linear correlation between them with a prefactor of 0.06. According to the mechanics of 1D blisters (*44*), the end-to-end compressive displacement $\Delta \sim \delta_e^2/\lambda_e$, combined with Eq. 6, Δ can be estimated by

$$\Delta \sim \frac{\lambda_e^3}{L_{ec}^2} \tag{7}$$

For an intact circular sheet with *N* different 2D blisters, the total hoop compression released by blistering is therefore the summation of the individual compressive displacement

$$\Delta_{total} = \sum_{i=1}^{N} \frac{\lambda_{e,i}^3}{L_{ec}^2} \tag{8}$$

Such hoop compression is induced by the geometric incompatibility between the flat sheets and the spherical substrates. Assuming no membrane strains, the following hoop compression must be accommodated (*47*)

$$\Delta_{total} = 2\pi\left(R - \rho\sin\frac{R}{\rho}\right) \sim \frac{R^3}{\rho^2} \tag{9}$$

where Taylor expansion is used.

Combining Eqs. 8 and 9, we can obtain the following scaling relation

$$\sum_{i=1}^{N} \lambda_{e,i}^3 \sim L_{ec}^2 \frac{R^3}{\rho^2} \tag{10}$$

To validate Eq. 10, we plot our experimental results in Fig. 4C, where we see a linear relation with a fitted coefficient of 58.8 and an R^2 of 0.92, which is within a reasonable range with the analytically derived coefficient of 41.4 assuming 1D blisters. Considering that the experimental system has imperfections in the PET sheets, stochastic conforming process, multistable states, and measurement uncertainties, an R^2 of 0.92 of the fitted results signifies a reasonable linear correlation. Therefore, a scaling law for λ_e is successfully obtained and validated.

The last missing scaling law is for *N*. Performing total energy minimization is a potential approach, but the energy close to the delamination fronts is difficult to estimate because of the complexity of the 3D curvature (*41*, *42*). Instead, we draw inspiration from another study. Xu *et al.* (*48*) have derived that the wrinkling wave number of a growing circular aquatic plant leaf floating on water is proportional to the leaf radius, i.e., $N_{wave} \sim R(\rho_w g/B)^{1/4}$, where ρ_w is the mass density of water and *g* is the gravitational acceleration. The characteristic length, $(B/\rho_w g)^{1/4}$, reveals that the critical wrinkling wave number of a circular floating lotus leaf is governed by the competition between the water pressure applied on the leaf and the bending stiffness of the leaf. On the basis of our experimental and numerical results, we found the following empirical relation for the number of blisters

$$N \sim \frac{R - r_c}{L(E, h, \gamma)} \sim \frac{R - r_c}{L_{ec}} \tag{11}$$

where $L(E, h, \gamma)$ is a length scale that controls the buckle formation and the buckle number. In our problem, the compression is induced by geometric mismatch instead of leaf growth, while the constraints come from the interface adhesion instead of the water pressure applied on the leaf. Therefore, we selected the elasto-capillary length to be our characteristic length, i.e., $L(E, h, \gamma) = L_{ec}$. This scaling law is plotted in Fig. 4D, which suggests a strong linear

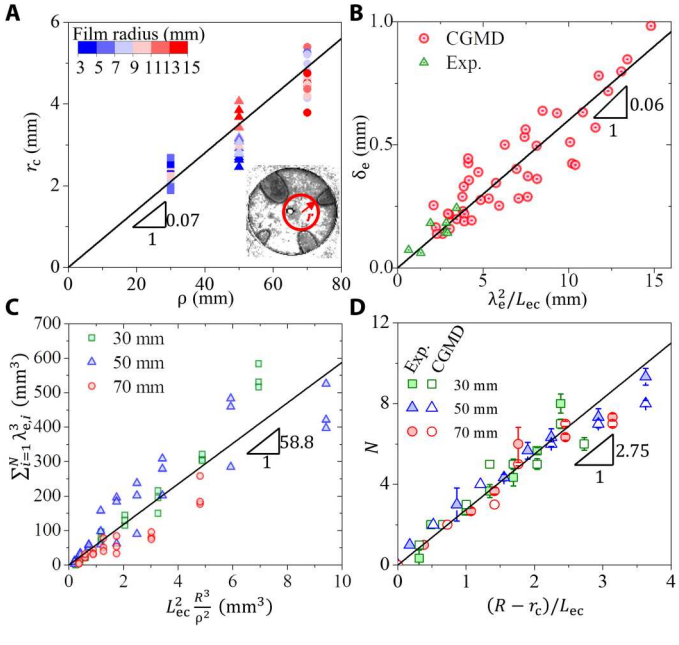

Fig. 4. Validations of scaling laws represented by black lines. (**A**) Validation of the scaling law in Eq. 5. (**B**) Validation of the scaling law in Eq. 6. (**C**) Validation of the scaling law in Eq. 10. (**D**) Validation of the scaling law in Eq. 11. Note that *N* in these aggregated results does not need to be an integer.

relation with a fitted coefficient of 2.75 and an R^2 of 0.98. Note that in both experiments (solid markers) and simulations (open markers), N varied from one test to another under the same condition. As a result, the markers in Fig. 4D can be non-integers and have error bars.

To validate this scaling law for various sheet thicknesses and moduli, we adopted the CGMD simulation as it has been validated by experiments. We performed simulations for fixed R = 9 mm and ρ = 30 mm, but varied E from 0.3 to 30 GPa and h from 3.25 to 52 μm. The maximum contact radius r_c in simulations was extracted and plotted against the prediction of Eq. 5 in Fig. 5A. Note that different from all other cases, the central region of the 52-μm-thick sheet failed to achieve full contact to the substrate after the water was fully drained. As a result, the maximum contact radius for this case is no longer located in the central region, as illustrated in Fig. 5D. It is validated that Eq. 5 can well predict the maximum contact radius r_c. The buckle number of these cases was counted and plotted in fig. S4, which deviates from the prediction of Eq. 11 when the sheet thickness or modulus is far from the 3 GPa or 13 μm, respectively. It indicates that the choice of $L(E, h, \gamma) = L_{ec}$ has limitations and a more rigorous relationship between N and R should be derived in the future. Although Eq. 11 cannot accurately predict the number of buckles for a wide range of sheet thicknesses and moduli, it highlights the linear relationship between N and $R - r_c$ in a limited regime of interest to this study. Besides, the buckle number has a limited effect on the delaminated area within the chosen thickness and modulus ranges because the delaminated area ($A_{blister}$) is proportional to $N^{\frac{2}{3}}$ by combining Eqs. 2, 3, and 10.

Conformability of intact sheets

With the scaling relations for r_c, λ_e, and N established, we are ready to estimate the conformability C. Assuming that N identical blisters appear for given sheet and substrate radii, the blisters have identical λ_e and extend from the edge of the sheet to r_c. Combining Eqs. 2 to 4, 10, and 11, we can obtain

$$C(R,\rho) = \begin{cases} 1 & ,R < r_c \\ 1 - \alpha\frac{(R-r_c)^{\frac{5}{3}}}{R\rho^{2/3}} & ,R > r_c \end{cases} \quad (12)$$

where α is an unknown coefficient. Normalizing R and r_c by ρ, we then obtain

$$C(\overline{R}) = \begin{cases} 1 & ,\overline{R} < \overline{r}_c \\ 1 - \alpha\frac{(\overline{R}-\overline{r}_c)^{\frac{5}{3}}}{\overline{R}} & ,\overline{R} > \overline{r}_c \end{cases} \quad (13)$$

where $\overline{R} = R/\rho$ is the only variable in this equation and $\overline{r}_c = 1.9(\gamma/Eh)^{1/4}$ is a dimensionless constant determined by material/interface properties, which equals 0.07 in our system. Equation 13 is plotted as the black curve in Fig. 2B with a fitted α = 1.75, which offers an excellent prediction of conformability when compared with experimental and simulation results. Equation 13 confirms our experimental/simulation observations (2) and (4) that R/ρ is the only controlling parameter for the conformability of a thin sheet to a rigid spherical surface and the two have a monotonic relationship. We also find that $\overline{r}_c$ is a good prediction of the critical size mentioned in observation (3), beyond which blisters will emerge to accommodate the geometric mismatches between a flat sheet and a spherical surface.

To investigate the effects of sheet modulus and thickness on conformability, we also plot the CGMD simulation results in Fig. 5 (B to D). It is evident that the conformability of the sheets can be well predicted by Eq. 13 for sheet modulus ranging from 0.3 to 30 GPa when sheet thickness is fixed to be 13 μm, as shown in Fig. 5B, and for sheet thickness ranging from 3.25 to 39 μm when sheet modulus is fixed to be 3 GPa, as shown in Fig. 5C. One exception is the sheet of 52-μm thickness and 3-GPa modulus, whose

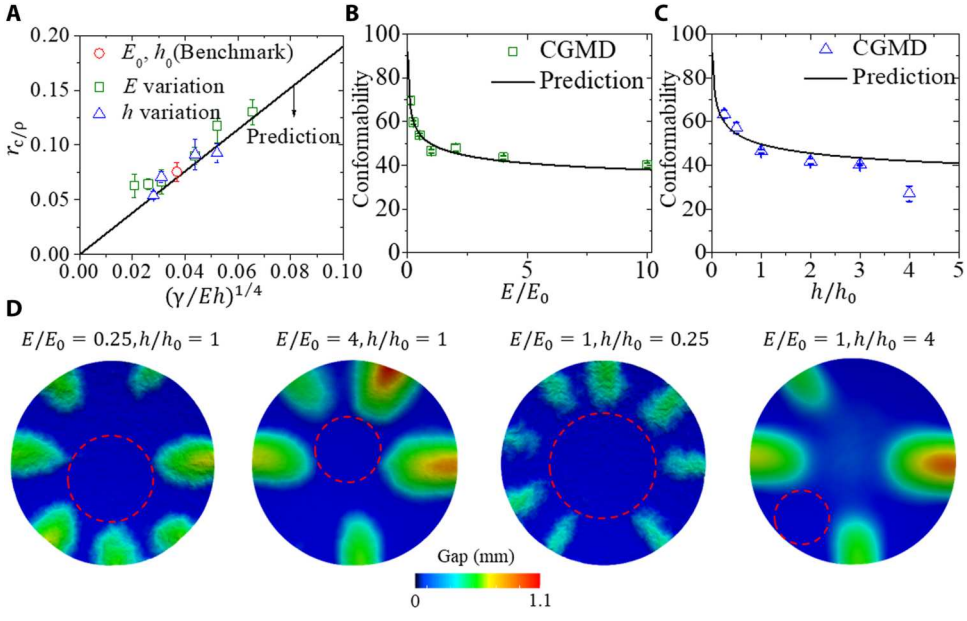

Fig. 5. Effects of sheet modulus and thickness. (**A**) Validation of the scaling law given by Eq. 5. (**B**) Validation of the scaling law given by Eq. 13 for different sheet moduli at a fixed sheet thickness of 13 μm. E_0 = 3 GPa. (**C**) Validation of the scaling law given by Eq. 13 for different sheet thicknesses at a fixed sheet modulus of 3 GPa. h_0 = 13 μm. (**D**) Four representative simulation results for different sheet moduli and sheet thicknesses. The red dashed circle in each case denotes the maximum contact radius.

center failed to conform to the substrate, as shown in movie S2. It indicates that Eq. 13 is not applicable to sheets whose bending energy has the same order of magnitude as the adhesion energy, i.e., $B\pi R^2/\rho^2 \sim \gamma\pi R^2$. In summary, the conformability prediction Eq. 13 is applicable when $B \ll \gamma\rho^2$.

Conformability enhancement by radial slits

For a circular sheet of radius R larger than r_c trying to conform to a spherical substrate of radius ρ, the formation of edge blisters is detrimental to conformability. As hoop compressive strain can be released by introducing radial slits (without removing any materials), it is the simplest alteration to the circular sheet to enhance conformability. Intuitively, more and longer slits are more effective. However, from the perspective of device integrity, which is critical for both circuit design and fabrication, it is useful to investigate how the conformability varies with cut number M and cut length l such that we can provide a rational guideline for the slit designs.

We first carried out experiments and CGMD modeling to quantify cut-facilitated conformability as summarized in Fig. 6. The experimental and numerical results are compared in Fig. 6A for three different cut-facilitated designs, (l, M) = (2 mm,3), (3 mm,2), (3 mm,3), for the configuration of R = 7 mm and ρ = 50 mm. It can be discovered that when M = 3, despite different l, all the big edge blisters disappear. However, when M = 2, one edge blister still exists, indicating that M = 3 is the minimum number of slits to eliminate edge blisters, i.e., M_{min}. The hoop compression that must be accommodated by each slit can be estimated as Δ_{total}/M_{min}, where Δ_{total} is the hoop compression induced by the intrinsic geometric mismatch as given in Eq. 9. Although all edge blisters disappear when M = 3, small conical blisters emerge at the tips of the slits because of the inward rotation of the slit edges to accommodate the hoop compression during conformation. Cone topology suggests that its apex angle is negatively correlated with the hoop compression released by it and positively correlated with the cut length,

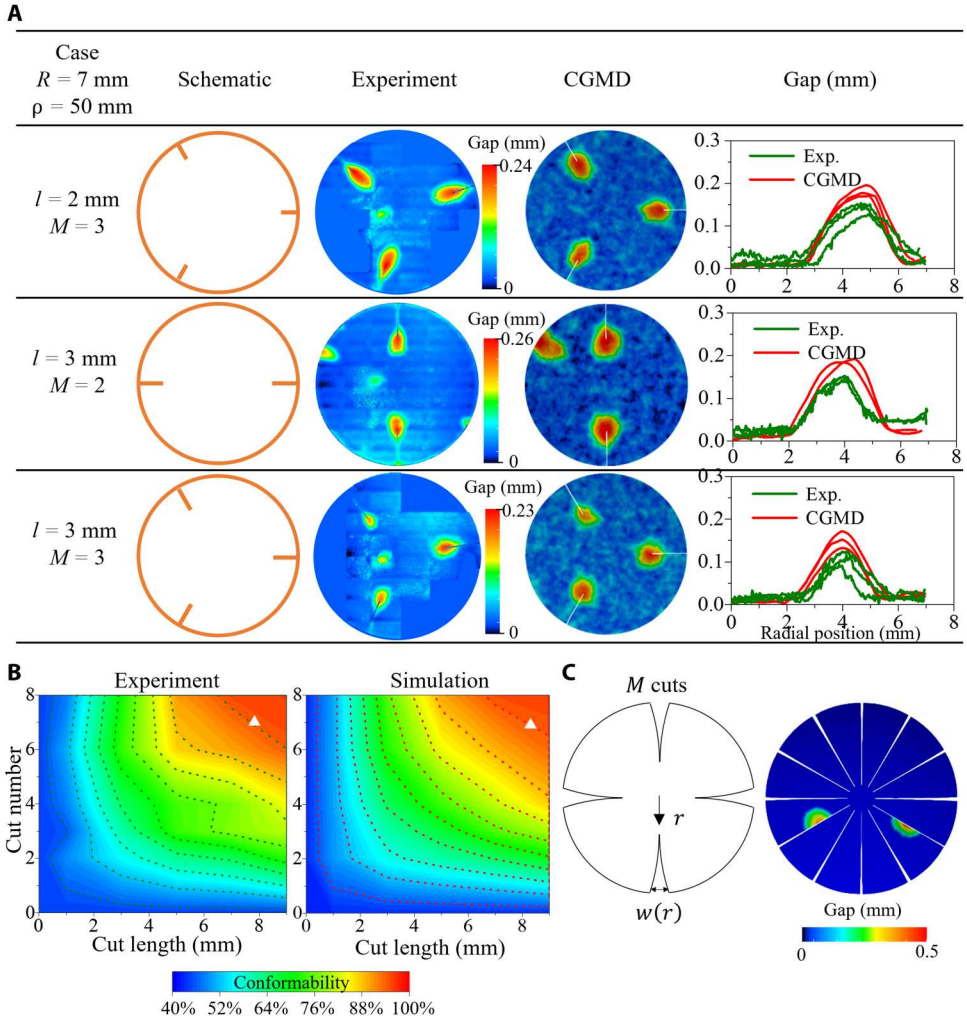

Fig. 6. Cut-facilitated conformability. (**A**) Schematics, 3D optical scans, and CGMD simulations for cut-facilitated designs with different cut lengths l and cut numbers M for the configuration of R = 7 mm and ρ = 50 mm. The last column plots the extracted sheet-substrate gap along the cuts from the sheet center, which is helpful for determining the sizes of the buckle delaminations at the tips of the slits. (**B**) Conformability variation with the cut number and the cut length in the experiment and simulation for the configuration of R = 10 mm and ρ = 30 mm. (**C**) The schematic (left) of curved cut design and simulated conformability result for R = 15 mm and ρ = 30 mm with 12 curved cuts.

as illustrated in fig. S5. If the apex angle is below a critical value, then the sheet-substrate interfacial adhesion is not strong enough to keep the sheet conformed, so the blister around the slit tip emerges. As a result, more cuts or longer cuts can lead to better global conformability. This is consistent with observations in the last column of Fig. 6A. When $M = 3$ is given, the sheet with $l = 2$ mm (row 1) exhibits larger (both width and height) slit tip blisters than the sheet with $l = 3$ mm (row 3). For fixed cut length ($l = 3$ mm), blisters with fewer slits ($M = 2$, row 2) have a larger slit tip blister height than the ones in $M = 3$ (row 3), although the edge blister in row 2 has already released some hoop compression.

Similar to intact sheets, we conducted experiments and CGMD simulations to systematically quantify the effects of the cut number and cut length. We selected the case of $R = 10$ mm and $\rho = 30$ mm as it has the worst conformability (44%) among all the cases that we studied. Optical images are displayed in fig. S3. We failed to handle sheets with $l = 9$ mm, $M = 6$ and $l = 9$ mm, $M = 8$ given their highly compromised integrity due to very long cuts. Three independent experiments and five independent simulations were carried out for each configuration, and the average conformability is summarized as contour plots for both experiments and simulations in Fig. 6B, where the horizontal axis represents the cut length, the vertical axis denotes the cut number, and the color indicates conformability. The two contour plots are within a 5% difference and verify that the conformability can be best enhanced when increasing both the length and the number of cuts. Fixing one and increasing the other can reach a plateau of conformability and hence is not the most effective.

Design strategies for optimal slits can be selected according to different criteria. To achieve 100% conformability, we just need to ensure that there is no intact zone with a radius exceeding r_c. So first, the slit must be cut starting from the edge and up to r_c

$$l = R - r_c \tag{14}$$

Then, the distance between two adjacent slits must be less than $2r_c$, so the cut number can be determined as

$$M = \frac{2\pi R}{2r_c} \tag{15}$$

This estimation would yield a large number of cuts, which corresponds to a conservative strategy that aims to achieve extreme conformability.

In practice, however, too many slits compromise device performance and increase handling difficulties. For example, given $R = 10$ mm and $\rho = 30$ mm, Eq. 14 suggests $l = 7.9$ mm, and Eq. 15 gives $M = 15$. However, in experiments, $M = 8$ was already difficult to handle in our experiments. An alternative design strategy is to aim for 90% conformability, which can be well achieved when $M = N$. According to Eq. 11, we can select

$$M = N = 2.75\frac{R - r_c}{L_{ec}} \tag{16}$$

where the coefficient came from fitting in Fig. 4D. This equation gives $M = 7$ for the case of $R = 10$ mm and $\rho = 30$ mm. From the contour plot in Fig. 6B, $M = 7$, $l = 8$ mm (white triangle) can give us a final conformability higher than 90% in both experiments and CGMD simulation. It is already a notable improvement compared with the intact circular sheet (44%). We performed CGMD simulation to examine whether Eq. 16 works for other geometric conditions. For two other cases of sheet and substrate radii $R = 14$ mm, $\rho = 50$ mm and $R = 14$ mm, $\rho = 70$ mm, nine cuts with 10.5-mm length and seven cuts with 9-mm length were derived from the second design guideline, respectively. We obtained conformability of 94.2 and 95.3% based on the CGMD simulation results.

Therefore, the guidelines for the cut-facilitated designs are summarized as follows: (i) Choose the cut length to be $R - r_c$. (ii) If 100% conformability is desired, then the cut number should be $\pi R/r_c$. (iii) If 90% conformability is adequate, the recommended cut number is $2.75(R - r_c)/L_{ec}$.

DISCUSSION

The conformability of a stiff thin sheet to a nondevelopable surface is practically meaningful for displays on 3D curved surfaces and body-conformable high-density electronics. In this study, we investigate the conformability of a flat circular sheet to a rigid spherical substrate with water-assisted conforming and adhesion. Experiments and CGMD simulations for various combinations of sheet and substrate radii were conducted to quantify not only the overall conformability but also the number and profiles of blisters. Mechanics-guided scaling laws were derived and validated. We first validated the radius of the maximum contact zone, $r_c = 1.9\rho(\gamma/Eh)^{1/4}$, beyond which edge blisters will form. Next, for film radius larger than r_c, we validated that the 2D blisters on spherical substrates can be regarded as quasi-1D blisters, and a scaling relation $N\lambda_e^3 \sim R^3L_{ec}^2/\rho^2$ can be derived on the basis of the knowledge of 1D blisters and the geometric confinement. We also found the number of blisters has a linear relationship with the sheet radius, $N \sim (R - r_c)/L_{ec}$. At last, the overall conformability can be estimated by a simple but nonlinear relation $C(R, \rho) = 1 - 1.75(R - r_c)^{5/3}/(R\rho^{2/3})$ for film radius larger than r_c when $B \ll \gamma\rho^2$. This fundamental discovery enables us to propose an easy-to-implement strategy to improve conformability through radial cuts without removing any materials from the sheet. While edge blisters can be eliminated by radial cuts, smaller blisters could form at the tips of the slits. The increasing cut number or increasing cut length can monotonically improve the conformability, although the enhancement is the most effective when the two increase together. Eventually, we propose a rational design guideline for the cut-facilitated conformability: $l = R - r_c$ for the cut length and $M = \pi R/r_c$ for the cut number if complete contact is desired, or $M = 2.75(R - r_c)/L_{ec}$ if 90% conformability is adequate.

Simple linear slits result in overlapping after the conformation, as shown in fig. S3. To avoid overlapping, we propose a curved cut design by removing some materials to match the hoop compression due to the conformation. Because the hoop compression is a function of r, the opening of each cut is therefore a function of r, as shown in the left schematic of Fig. 6C. On the basis of our design guidelines, the cut must start from $r = r_c$, so we obtained

$$w(r) = \begin{cases} 0 & r \le r_c \\ 0.73\pi L_{ec}\frac{r - \rho\sin\frac{r}{\rho}}{R - r_c} & r > r_c \end{cases} \tag{17}$$

Simulation is performed to validate this design for $R = 15$ mm and $\rho = 30$ mm with 12 curved cuts following Eq. 17. Its conforming process is shown in movie S3, and the final conformability is shown

in Fig. 6C (right). Compared with Fig. 6A, blisters at the tips of the cuts disappear. Although two edge blisters emerge, the overall conformability can still reach 96.5%.

In this study, we examined the conformability and methods for enhancing conformability of flexible sheets on a rigid spherical surface. The findings of this work can be used as a conservative estimate for conformability on soft substrates, which have the ability to deform and adapt to the electronics. The conformability would be higher when substrate radius of Gaussian curvature is larger than the undeformed configuration. However, predicting the exact 3D conformability on soft, nondevelopable surfaces requires more in-depth research. A 2D analysis of conformability on soft substrate has been demonstrated in our previous study (*49*).

MATERIALS AND METHODS

Experimental setup and the conforming process

The setup of a single experiment consists of a circular PET sheet, about 10 ml of black ink, and a hemispherical plastic shell as the rigid substrate. To ensure the flatness of the PET sheets and avoid folding during fabrication, laser cutting was used to pattern circles with different radii on a large PET sheet. To enable ink draining for fast conforming, a 0.8-mm-diameter hole was drilled at the center of the plastic shells. A customized pipette was developed to control the draining pressure and drain the excessive ink from the plastic shell through the hole. The draining pipette was customized by gluing a suction cup at the tip of a plastic transfer pipette. The suction cup guaranteed intimate contact between the pipette and the plastic shell for a smoother draining process. As a result, the draining process is controllable.

The conforming process is illustrated in Fig. 1D. First, 10 ml of black ink was added to the concave side of the hemispherical shell, and a circular sheet was placed on the ink surface. Because of the surface tension, the ink cannot leak from the small draining hole. Second, the draining pipette was applied to the outer surface of the hemispherical shell and kept draining for 30 s. Third, the draining pipette was gently slipped away from the draining hole and then removed from the hemispherical shell. Last, after the circular sheet achieves a stable state, the plastic shell with a circular sheet was placed on a lighting panel. The optical images were taken from the top-down view. For each geometry, three independent experiments were run to obtain the average conformability.

Image processing

A MATLAB code was programmed to process the images and estimate the conformability of the PET sheet. The optical images were first cropped to remove unnecessary regions, so the code only focuses on the sheet region for processing time reduction. Then, the full-color space of the images was converted to grayscale, and the region growth function (*50*) was implemented to capture the delaminated region. After that, binary pictures with black and white colors only were generated to show the status of in-contact or out-of-contact, respectively. At last, the contact area can be calculated pixel by pixel. The wavelength of buckle delamination was measured manually from the optical images.

Height profile by 3D scanning

Although the wavelength and the conformability can be measured from the optical images in experiments, we cannot obtain the out-of-plane deflection of the thin sheet. The height profiles in Fig. 3A and fig. S1A were measured by an optical profilometer (Keyence VK-X1100), but it cannot be conducted for arbitrary geometry of sheet and substrate due to the height limitation. Therefore, we only investigated sheets of two different radii R = 5 and 7 mm on a substrate of 50-mm radius. Because nontransparent objects are required for laser scan, the experimental setup was modified. An ultrathin layer of black ink was spray-coated and dried on the PET sheets to colorize the sheets. The hemispherical shell was cut into a spherical cap with a height of 5 mm and could be scanned under low magnification. The 3D scanning must be finished within 30 min to ensure the attachment of the sheet to the spherical cap because the laser accelerates the water evaporation and introduces thermal perturbation to the system, which can significantly affect the buckling morphology if water is completely evaporated.

After the height profile was obtained, postprocessing of the height profile data was performed. First, the few missing height data due to scanning errors were filled by interpolating neighboring data. Second, the spherical substrate was identified on the basis of the sheet regions in full contact. Last, we subtracted the spherical substrate from the height profile, so the contour plot of the gap between the sheet and the substrate was obtained.

MD simulation

For complicated contact problems, convergence is a challenge for the finite element method and usually requires high computational costs. Hence, we selected CGMD to simulate the sheet-conforming process in the experiment. Both the sheet and substrate are explicitly modeled in the simulation, but water is implicitly considered to further reduce the computational cost. Both the sheet and substrate are modeled by lattice-spring models. The driving force of the conforming process comes from water drainage, so an equivalent uniformly distributed load is first applied in a circular region and then removed after the sheet contacts the substrate. In the following subsections, we briefly introduce the methods and models for the sheet, substrate, water, and their interactions.

Lattice-spring model

The sheet is modeled by a series of interactive particles x_i ($i \in 1 \cdots N_v$), which forms N_s bonds and N_t triangular elements, as shown in fig. S6A (*39*, *51*–*53*). The mechanical property of the sheet is governed by the area potential V_{area}, volume potential V_{volume}, in-plane stretching potential $V_{in-plane}$, and bending potential $V_{bending}$. The total potential energy of the sheet can then be described as

$$V_{(x_i)} = V_{area} + V_{volume} + V_{in-plane} + V_{bending} \quad (18)$$

As shown in fig. S6B, the in-plane stretching of the sheet is modeled by the length variation of particle bonds, so the stretching energy $V_{in-plane}$ can be expressed by

$$V_{in-plane} = \sum_{i \in 1 \cdots N_s} k_s \, (l_i - l_{i0})^2 \quad (19)$$

where k_s is the stretching spring constant and l_i and l_{i0} are the current spring length and its original length in equilibrium.

The area potential energy V_{area} is used to constrain the area change of the sheet that reflects the conservation of surface area

for the sheet

$$V_{\text{area}} = \frac{k_a\ (A - A_{T0})^2}{2A_{T0}} + \sum_{i\in 1\cdots N_t} \frac{k_d\ (A_i - A_0)^2}{2A_0} \quad (20)$$

where k_a and k_d are the global and local area constraint coefficients, respectively, A and A_{T0} are the total area and the original total area of the sheet, respectively, and A_i and A_0 are the area element and the original area of each triangular element, respectively. Note that the area potential energy V_{area} consists of two parts: The first term constrains the total area of the entire sheet; the second term regulates the local area of each element. In addition, the relationship between the in-plane stretching modulus K of the particle sheet and the global area k_a, local area constraints coefficients k_d, and spring constant k_s can be derived as (*54*, *55*)

$$K = k_a + k_d + \sqrt{3}k_s \quad (21)$$

The volume potential V_{volume} is used to control the volume change

$$V_{\text{volume}} = \frac{k_v\ (V - V_{K0})^2}{2V_{K0}} \quad (22)$$

where k_v is the volume constraint coefficient and V and V_{K0} are the total volume and the original volume of the sheet, respectively.

The bending energy can be described by the variation of the dihedral angle between two adjacent elements, as shown in fig. S6C. The bending potential $V_{bending}$

$$V_{\text{bending}} = \sum_{i\in 1\cdots N_s} k_{\text{bend}}\ [1 - \cos(\theta_i - \theta_{i0})] \quad (23)$$

where k_{bend} is the bending constant, θ_i is the dihedral angle between two adjacent elements with shared edge i, and θ_{i0} is the original dihedral angle. Note that the bending constant k_{bend} is associated with the macroscopic bending rigidity B of the sheet based on the Helfrich model (*54*, *55*), which can be written as $B = \sqrt{3}k_{bend}/2$. In our study, the sheet thickness is far less than the sheet radius, so the contribution of V_{volume} is negligible. Existing studies also show that the sheet buckling can be well captured even not considering the area constraint V_{area} (*56*, *57*). Therefore, in our simulation, we only consider the in-plane stretching $V_{in-plane}$ and bending $V_{bending}$ in the total potential energy. The sheet elasticity is governed by the bending constant k_{bend} and stretching constant k_s of the lattice-spring model. The motion of all particles obeys Newtonian mechanics.

Coarse-grained molecular dynamics

CGMD simulation has proved its capability in simulating both the large-scale continuum mechanics and the atomistic Monte Carlo simulations (*58*–*60*), such as calculating the elastic constants (*61*), simulating the deformation of an origami plate (*62*), and simulating the transport of nanoparticle-based drug carriers in blood flow (*39*). Therefore, we performed CGMD with the large-scale atomic molecular massively parallel simulator (*63*) to model the conforming of thin sheets to spherical substrates.

In the CGMD model, the substrate was modeled by a spherical thin shell consisting of the discretized particles, and these particles were uniformly distributed on the spherical surface using the method proposed by Deserno (*64*), as shown in Fig. 1E. The substrate serves as a rigid body in the experiment, so all the potential energies among the interactive particles of the substrate are neglected. The circular sheet modeled by the lattice-spring model was placed on the top of a hemispherical container and parallel to the X-Y plane. Then, a uniformly distributed load was applied around the center of the sheet to model the driving force from the water. As the sheet gradually conformed to the substrate, the distributed load was removed, but the conforming of the sheet continued because of the existence of gravity, inertia, and adhesion. To simulate the adhesion provided by interfacial water, the Lennard-Jones potential with parameters σ and ϵ is used and calibrated.

Constant temperature CGMD simulations were carried out at 300 K using the canonical ensemble (NVT) with a Langevin thermostat with a time step of 0.1. A gravity load was imposed on each particle. The cutoff parameter was set to be 2σ for the Lennard-Jones potential. After the sheet conforms to the substrate, the simulation kept running for 2×10^7 time steps, which is long enough to achieve equilibrium. When the total energy achieves equilibrium, the sheet morphology was considered as its final stable morphology. It was used in the subsequent analysis, including conformability calculation, wavelength, and amplitude measurement for each buckle delamination. In addition, to eliminate the random velocity effect, five independent models with different initial velocities are performed for each combination of sheet and substrate radii. The final quantitative results for each configuration were obtained by averaging the results of the five independent models.

To perform the CGMD simulation, it is crucial to correctly determine the parameters of the properties based on the macroscopic properties of the physical system. For example, the stretching spring constant can be determined by k_s and the bending constant is calibrated from experiments. Details can be found in the Supplementary Materials. In addition, the effect of mesh size was checked, and a 0.2-mm mesh size was selected to perform all CGMD simulations. To avoid unexpected fluctuations affecting our results, the final stable morphology was defined as the average morphology of the last 50 steps. Details about the mesh convergence study can be found in the Supplementary Materials.

Supplementary Materials

This PDF file includes:

Supplementary Text
Figs. S1 to S9
Tables S1 to S4
Legends for movies S1 to S3

Other Supplementary Material for this manuscript includes the following:

Movies S1 to S3

REFERENCES AND NOTES

1. Y. Huang, H. Wu, L. Xiao, Y. Duan, H. Zhu, J. Bian, D. Ye, Z. Yin, Assembly and applications of 3D conformal electronics on curvilinear surfaces. *Mater. Horiz.* **6**, 642–683 (2019).
2. S. Liu, Y. Rao, H. Jang, P. Tan, N. Lu, Strategies for body-conformable electronics. *Matter* **5**, 1104–1136 (2022).
3. S. Yang, Y. C. Chen, L. Nicolini, P. Pasupathy, J. Sacks, B. Su, R. Yang, D. Sanchez, Y. F. Chang, P. Wang, "Cut-and-paste" manufacture of multiparametric epidermal sensor systems. *Adv. Mater.* **27**, 6423–6430 (2015).
4. S. Jiang, J. Liu, W. Xiong, Z. Yang, L. Yin, K. Li, Y. Huang, A Snakeskin-inspired, Soft-Hinge Kirigami metamaterial for self-adaptive conformal electronic armor. *Adv. Mater.* **34**, 2204091 (2022).

5. Y. Kim, C. Zhu, W.-Y. Lee, A. Smith, H. Ma, X. Li, D. Son, N. Matsuhisa, J. Kim, W.-G. Bae, S. H. Cho, M.-G. Kim, T. Kurosawa, T. Katsumata, J. W. F. To, J. Y. Oh, S. Paik, S. J. Kim, L. Jin, F. Yan, J. B.-H. Tok, Z. Bao, A hemispherical image sensor array fabricated with organic photo-memory transistors. *Adv. Mater.* **35**, e2203541 (2022).
6. K. Zhang, Y. H. Jung, S. Mikael, J.-H. Seo, M. Kim, H. Mi, H. Zhou, Z. Xia, W. Zhou, S. Gong, Z. Ma, Origami silicon optoelectronics for hemispherical electronic eye systems. *Nat. Commun.* **8**, 1782 (2017).
7. D. H. Kim, N. Lu, R. Ma, Y. S. Kim, R. H. Kim, S. Wang, J. Wu, S. M. Won, H. Tao, A. Islam, K. J. Yu, T. I. Kim, R. Chowdhury, M. Ying, L. Xu, M. Li, H. J. Chung, H. Keum, M. McCormick, P. Liu, Y. W. Zhang, F. G. Omenetto, Y. Huang, T. Coleman, J. A. Rogers, Epidermal electronics. *Science* **333**, 838–843 (2011).
8. D. H. Kim, J. Viventi, J. J. Amsden, J. Xiao, L. Vigeland, Y. S. Kim, J. A. Blanco, B. Panilaitis, E. S. Frechette, D. Contreras, D. L. Kaplan, F. G. Omenetto, Y. Huang, K. C. Hwang, M. R. Zakin, B. Litt, J. A. Rogers, Dissolvable films of silk fibroin for ultrathin conformal bio-integrated electronics. *Nat. Mater.* **9**, 511–517 (2010).
9. I. R. Minev, P. Musienko, A. Hirsch, Q. Barraud, N. Wenger, E. M. Moraud, J. Gandar, M. Capogrosso, T. Milekovic, L. Asboth, R. F. Torres, N. Vachicouras, Q. Liu, N. Pavlova, S. Duis, A. Larmagnac, J. Voros, S. Micera, Z. Suo, G. Courtine, S. P. Lacour, Electronic dura mater for long-term multimodal neural interfaces. *Science* **347**, 159–163 (2015).
10. J. Park, J. Kim, S.-Y. Kim, W. H. Cheong, J. Jang, Y.-G. Park, K. Na, Y.-T. Kim, J. H. Heo, C. Y. Lee, J. H. Lee, F. Bien, J.-U. Park, Soft, smart contact lenses with integrations of wireless circuits, glucose sensors, and displays. *Sci. Adv.* **4**, eaap9841 (2018).
11. C. Choi, M. K. Choi, S. Liu, M. S. Kim, O. K. Park, C. Im, J. Kim, X. Qin, G. J. Lee, K. W. Cho, M. Kim, E. Joh, J. Lee, D. Son, S.-H. Kwon, N. L. Jeon, Y. M. Song, N. Lu, D.-H. Kim, Human eye-inspired soft optoelectronic device using high-density MoS_2-graphene curved image sensor array. *Nat. Commun.* **8**, 1664 (2017).
12. J. W. Jeong, W. H. Yeo, A. Akhtar, J. J. Norton, Y. J. Kwack, S. Li, S. Y. Jung, Y. Su, W. Lee, J. Xia, H. Cheng, Y. Huang, W. S. Choi, T. Bretl, J. A. Rogers, Materials and optimized designs for human-machine interfaces via epidermal electronics. *Adv. Mater.* **25**, 6839–6846 (2013).
13. F. Ershad, A. Thukral, J. Yue, P. Comeaux, Y. Lu, H. Shim, K. Sim, N. I. Kim, Z. Rao, R. Guevara, L. Contreras, F. Pan, Y. Zhang, Y. S. Guan, P. Yang, X. Wang, P. Wang, X. Wu, C. Yu, Ultra-conformal drawn-on-skin electronics for multifunctional motion artifact-free sensing and point-of-care treatment. *Nat. Commun.* **11**, 3823 (2020).
14. C. F. Gauss, *General Investigations of Curved Surfaces of 1827 and 1825* (Princeton Univ. Library, 1902).
15. S. Wang, M. Li, J. Wu, D.-H. Kim, N. Lu, Y. Su, Z. Kang, Y. Huang, J. A. Rogers, Mechanics of epidermal electronics. *J. Appl. Mech.* **79**, 031022 (2012).
16. N. Lu, S. Yang, Mechanics for stretchable sensors. *Curr. Opin. Solid State Mater. Sci.* **19**, 149–159 (2015).
17. T. Q. Trung, N. E. Lee, Recent progress on stretchable electronic devices with intrinsically stretchable components. *Adv. Mater.* **29**, 1603167 (2017).
18. Y. G. Park, G. Y. Lee, J. Jang, S. M. Yun, E. Kim, J. U. Park, Liquid metal-based soft electronics for wearable healthcare. *Adv. Healthc. Mater.* **10**, e2002280 (2021).
19. X. Sun, F. Yao, J. Li, Nanocomposite hydrogel-based strain and pressure sensors: A review. *J. Mater. Chem. A* **8**, 18605–18623 (2020).
20. K. I. Jang, H. U. Chung, S. Xu, C. H. Lee, H. Luan, J. Jeong, H. Cheng, G. T. Kim, S. Y. Han, J. W. Lee, J. Kim, M. Cho, F. Miao, Y. Yang, H. N. Jung, M. Flavin, H. Liu, G. W. Kong, K. J. Yu, S. I. Rhee, J. Chung, B. Kim, J. W. Kwak, M. H. Yun, J. Y. Kim, Y. M. Song, U. Paik, Y. Zhang, Y. Huang, J. A. Rogers, Soft network composite materials with deterministic and bio-inspired designs. *Nat. Commun.* **6**, 6566 (2015).
21. Z. Rao, Y. Lu, Z. Li, K. Sim, Z. Ma, J. Xiao, C. Yu, Curvy, shape-adaptive imagers based on printed optoelectronic pixels with a kirigami design. *Nat. Electron.* **4**, 513–521 (2021).
22. Y. Morikawa, S. Yamagiwa, H. Sawahata, R. Numano, K. Koida, M. Ishida, T. Kawano, Ultrastretchable Kirigami bioprobes. *Adv. Healthc. Mater.* **7**, 1701100 (2018).
23. H. C. Ko, M. P. Stoykovich, J. Song, V. Malyarchuk, W. M. Choi, C. J. Yu, J. B. Geddes III, J. Xiao, S. Wang, Y. Huang, J. A. Rogers, A hemispherical electronic eye camera based on compressible silicon optoelectronics. *Nature* **454**, 748–753 (2008).
24. P. Won, S. Jeong, C. Majidi, S. H. Ko, Recent advances in liquid-metal-based wearable electronics and materials. *iScience* **24**, 102698 (2021).
25. Y. Zhang, S. Xu, H. Fu, J. Lee, J. Su, K. C. Hwang, J. A. Rogers, Y. Huang, Buckling in serpentine microstructures and applications in elastomer-supported ultra-stretchable electronics with high areal coverage. *Soft Matter* **9**, 8062–8070 (2013).
26. K. Sim, S. Chen, Z. Li, Z. Rao, J. Liu, Y. Lu, S. Jang, F. Ershad, J. Chen, J. Xiao, C. Yu, Three-dimensional curvy electronics created using conformal additive stamp printing. *Nat. Electron.* **2**, 471–479 (2019).
27. J. Liu, S. Jiang, W. Xiong, C. Zhu, K. Li, Y. Huang, Self-healing Kirigami assembly strategy for conformal electronics. *Adv. Funct. Mater.* **32**, 2109214 (2022).
28. Y.-K. Lee, Z. Xi, Y.-J. Lee, Y.-H. Kim, Y. Hao, H. Choi, M.-G. Lee, Y.-C. Joo, C. Kim, J.-M. Lien, I.-S. Choi, Computational wrapping: A universal method to wrap 3D-curved surfaces with nonstretchable materials for conformal devices. *Sci. Adv.* **6**, eaax6212 (2020).
29. Y.-J. Lee, S. K. Kanchwala, H. Cho, J. C. Jolly, E. Jablonka, M. Tanis, R. D. Kamien, S. Yang, Natural shaping of acellular dermal matrices for implant-based breast reconstruction via expansile Kirigami. *Adv. Mater.* **35**, e2208088
30. J. Hure, B. Roman, J. Bico, Wrapping an adhesive sphere with an elastic sheet. *Phys. Rev. Lett.* **106**, 174301 (2011).
31. C. Majidi, R. S. Fearing, Adhesion of an elastic plate to a sphere. *Proc. R. Soc. A Math. Phys. Eng. Sci.* **464**, 1309–1317 (2008).
32. J. Hure, B. Audoly, Capillary buckling of a thin film adhering to a sphere. *J. Mech. Phys. Solids* **61**, 450–471 (2013).
33. Y. Chen, Y. Ma, S. Wang, Y. Zhou, H. Liu, The morphology of graphene on a non-developable concave substrate. *Appl. Phys. Lett.* **108**, 031905 (2016).
34. F. Box, L. Domino, T. O. Corvo, M. Adda-Bedia, V. Démery, D. Vella, B. Davidovitch, Delamination from an adhesive sphere: Curvature-induced dewetting versus buckling. arXiv:2207.07927 [cond-mat.soft] (2022).
35. S. Kabiri Ameri, R. Ho, H. Jang, L. Tao, Y. Wang, L. Wang, D. M. Schnyer, D. Akinwande, N. Lu, Graphene electronic tattoo sensors. *ACS Nano* **11**, 7634–7641 (2017).
36. B. Le Borgne, S. Liu, X. Morvan, S. Crand, R. A. Sporea, N. Lu, M. Harnois, Water transfer printing enhanced by water-induced pattern expansion: Toward large-area 3D electronics. *Adv. Mater. Technol.* **4**, 1800600 (2019).
37. T. Sekitani, U. Zschieschang, H. Klauk, T. Someya, Flexible organic transistors and circuits with extreme bending stability. *Nat. Mater.* **9**, 1015–1022 (2010).
38. T. Sekitani, S. Iba, Y. Kato, Y. Noguchi, T. Someya, T. Sakurai, Ultraflexible organic field-effect transistors embedded at a neutral strain position. *Appl.Phys. Lett.* **87**, 173502 (2005).
39. H. Ye, Z. Shen, Y. Li, Computational modeling of magnetic particle margination within blood flow through LAMMPS. *Comput. Mech.* **62**, 457–476 (2018).
40. H. Ye, Z. Shen, W. Xian, T. Zhang, S. Tang, Y. Li, OpenFSI: A highly efficient and portable fluid–structure simulation package based on immersed-boundary method. *Comput. Phys. Commun.* **256**, 107463 (2020).
41. J. Chopin, D. Vella, A. Boudaoud, The liquid blister test. *Proc. R. Soc. A Math. Phys. Eng. Sci.* **464**, 2887–2906 (2008).
42. Y. Aoyanagi, J. Hure, J. Bico, B. Roman, Random blisters on stickers: Metrology through defects. *Soft Matter* **6**, 5720–5728 (2010).
43. R. D. Schroll, E. Katifori, B. Davidovitch, Elastic building blocks for confined sheets. *Phys. Rev. Lett.* **106**, 074301 (2011).
44. B. Davidovitch, V. Démery, Rucks and folds: Delamination from a flat rigid substrate under uniaxial compression. *Eur. Phys. J. E* **44**, 11 (2021).
45. G. M. Grason, B. Davidovitch, Universal collapse of stress and wrinkle-to-scar transition in spherically confined crystalline sheets. *Proc. Natl. Acad. Sci. U.S.A.* **110**, 12893–12898 (2013).
46. E. Hohlfeld, B. Davidovitch, Sheet on a deformable sphere: Wrinkle patterns suppress curvature-induced delamination. *Phys. Rev. E* **91**, 012407 (2015).
47. B. Davidovitch, Y. Sun, G. M. Grason, Geometrically incompatible confinement of solids. *Proc. Natl. Acad. Sci. U.S.A.* **116**, 1483–1488 (2019).
48. F. Xu, C. Fu, Y. Yang, Water affects morphogenesis of growing aquatic plant leaves. *Phys. Rev. Lett.* **124**, 038003 (2020).
49. L. Wang, S. Qiao, S. Kabiri Ameri, H. Jeong, N. Lu, A thin elastic membrane conformed to a soft and rough substrate subjected to stretching/compression. *J. Appl. Mech.* **84**, 111003 (2017).
50. D.-J. Kroon (2022); https://www.mathworks.com/matlabcentral/fileexchange/19084-region-growing.
51. Z. Shen, H. Ye, Y. Li, Understanding receptor-mediated endocytosis of elastic nanoparticles through coarse grained molecular dynamic simulation. *Phys. Chem. Chem. Phys.* **20**, 16372–16385 (2018).
52. J. Li, M. Dao, C. T. Lim, S. Suresh, Spectrin-level modeling of the cytoskeleton and optical tweezers stretching of the erythrocyte. *Biophys. J.* **88**, 3707–3719 (2005).
53. D. A. Fedosov, B. Caswell, G. E. Karniadakis, Systematic coarse-graining of spectrin-level red blood cell models. *Comput. Methods Appl. Mech. Eng.* **199**, 1937–1948 (2010).
54. D. A. Fedosov, *Multiscale Modeling of Blood Flow and Soft Matter* (Brown Univ., 2010).
55. D. A. Fedosov, B. Caswell, G. E. Karniadakis, A multiscale red blood cell model with accurate mechanics, rheology, and dynamics. *Biophys. J.* **98**, 2215–2225 (2010).
56. P. Z. Hanakata, S. S. Bhabesh, M. J. Bowick, D. R. Nelson, D. Yllanes, Thermal buckling and symmetry breaking in thin ribbons under compression. *Extreme Mech. Lett.* **44**, 101270 (2021).
57. A. Morshedifard, M. Ruiz-García, M. J. Abdolhosseini Qomi, A. Košmrlj, Buckling of thermalized elastic sheets. *J. Mech. Phys. Solids* **149**, 104296 (2021).

58. J. H. Los, A. Fasolino, M. I. Katsnelson, Scaling behavior and strain dependence of in-plane elastic properties of graphene. *Phys. Rev. Lett.* **116**, 015901 (2016).
59. R. Zhao, Y. Kim, S. A. Chester, P. Sharma, X. Zhao, Mechanics of hard-magnetic soft materials. *J. Mech. Phys. Solids* **124**, 244–263 (2019).
60. S. Suresh, J. Spatz, J. P. Mills, A. Micoulet, M. Dao, C. T. Lim, M. Beil, T. Seufferlein, Reprint of: Connections between single-cell biomechanics and human disease states: Gastrointestinal cancer and malaria. *Acta Biomater.* **23**, S3–S15 (2015).
61. K. Bertoldi, V. Vitelli, J. Christensen, M. van Hecke, Flexible mechanical metamaterials. *Nat. Rev. Mater.* **2**, 17066 (2017).
62. H. Ye, Y. Li, T. Zhang, Magttice: A lattice model for hard-magnetic soft materials. *Soft Matter* **17**, 3560–3568 (2021).
63. S. Plimpton, Fast parallel algorithms for short-range molecular dynamics. *J. Comput. Phys.* **117**, 1–19 (1995).
64. M. Deserno, *How to Generate Equidistributed Points on the Surface of a Sphere* (Max-Planck-Institut fur Polymerforschung, 2004).

Acknowledgments
Funding: N.L. acknowledges the support from the U.S. Army Research Office under Cooperative Agreement W911NF-19-2-0333, and the NSF under grant 2133106. Y.L. would like to thank the support from the NSF under grants 1755779, 1762661, and 1934829, as well as 3M's Non-Tenured Faculty Award. **Author contributions:** Conceptualization: S.L. and N.L. Experiments: S.L. and J.C.T. Analysis: S.L., Y.R., Z.D., and N.L. Simulation: J.H., H.Y., and Y.L. Visualization: S.L. and J.H. Supervision and funding: N.L. and Y.L. Writing (original draft): S.L., J.H., and N.L. Writing (review and editing): N.L., Y.L., S.L., and J.H. **Competing interests:** The authors declare that they have no competing interests. **Data and materials availability:** All data needed to evaluate the conclusion in the paper are present in the paper and/or the Supplementary Materials.

Submitted 11 October 2022
Accepted 20 March 2023
Published 19 April 2023
10.1126/sciadv.adf2709

ScienceAdvances

Conformability of flexible sheets on spherical surfaces

Siyi Liu, Jinlong He, Yifan Rao, Zhaohe Dai, Huilin Ye, John C. Tanir, Ying Li, and Nanshu Lu

Sci. Adv., **9** (16), eadf2709.
DOI: 10.1126/sciadv.adf2709

Science Advances (ISSN) is published by the American Association for the Advancement of Science. 1200 New York Avenue NW, Washington, DC 20005. The title *Science Advances* is a registered trademark of AAAS.

Science Advances
AAAS

Supplementary Materials for

Conformability of flexible sheets on spherical surfaces

Siyi Liu *et al.*

Corresponding author: Nanshu Lu, nanshulu@utexas.edu; Ying Li, yli2562@wisc.edu

Sci. Adv. **9**, eadf2709 (2023)
DOI: 10.1126/sciadv.adf2709

The PDF file includes:

Other Supplementary Material for this manuscript includes the following:

1. Curved Design of the Cut

For cut-facilitated design, the cut opening can be nonlinear for better coverage on the target substrate. The cut opening can be estimated by pure geometric relations. Assuming no radial stretching applied on the thin sheet, the entire sheet is subjected to hoop compression, which is a function of the radial coordinate r. Equation (9) offers the total hoop compression

$$\Delta(r) = 2\pi\left(r - \rho \sin\frac{r}{\rho}\right) \tag{S1}$$

If the cut is a simple parallel narrow slit, such a compression induces sheet overlapping instead of buckle delamination, as shown in **Fig. S3**. Here, we propose a curved design to achieve a high coverage without overlapping by considering the hoop compression in Eq. (S1). Assuming M cuts of length l are made to improve the conformability of a sheet of radius $R > r_c$, we can obtain the slit opening, *i.e.*, the material to be removed at each cut is

$$w(r) = \frac{\Delta(r)}{M} = \frac{2\pi\left(r-\rho \sin\frac{r}{\rho}\right)}{M} \tag{S2}$$

Using the 90% conformability strategy Eq. (16), the cut opening can be obtained

$$w(r) = \begin{cases} 0 & r < r_c \\ 0.73\pi L_{\mathrm{ec}} \frac{r-\rho \sin\frac{r}{\rho}}{R-r_c} & r > r_c \end{cases} \tag{S3}$$

It indicates that the cut starts at $r = r_c$ and is curved as shown in **Fig. 6C**. Simulation is performed to validate this design for a sheet with a radius of 15 mm conformed to a spherical surface of a radius of 30 mm, as shown in **Fig. 6C**. The thin sheet has 12 curved slits of 12.9 mm long. It conformed well to the spherical substrate, and its conformability is 96% without any overlapping. **Movie S3** shows the entire conforming process and final morphology in simulation.

2. Model Calibration and Reduced-Scale Structural Model

For thin-sheet structures, on the macroscopic scale, finite element methods usually have difficulties in separating the contribution of different deformation types, e.g., stretching and bending. Hence, molecular dynamics (MD) simulations are more suitable to model the water-assisted transfer process. However, using MD simulations at a

microscopic scale can be time-consuming and costly due to the large number of atoms and the small timestep for integration. To overcome these challenges, the experimental setup was first scaled to the atomic scale, and then a particle-based coarse-grained approach was employed to model the deformable sheet at the atomic scale in this work. Following coarse-grained molecular dynamics (CGMD), one particle can represent a part of the scaled sheet to reduce the degrees of freedom in the system. The mechanical properties in both simulation and physical space are listed in **Table S1**.

Table S1 Material parameters used in CGMD and their corresponding physical values

Parameters	Simulation	Physical
Length scale	1	1×10^{-4} m
Force scale	1	1.70×10^{-3} N
Surface tension	3.970×10^{-3}	7.200×10^{-2} N m^{-1}
Adhesion energy	7.940×10^{-3}	1.440×10^{-1} N m^{-1}
Stretching constant	1500	2.546×10^{4} N m^{-1}
Bending constant	4.313	7.171×10^{-7} N m

Since the unit system in simulation (e.g., time, temperature, amount of substance, length, etc.) is totally different from the physical values in the experiments, a calibration of the material parameters is required. Three key material properties, the sheet bending rigidity, stretching stiffness, and adhesion energy, must be correctly converted in the simulation because they are governing the buckling delaminations. The material parameters in our simulation were calibrated based on a top-down method to achieve experimental observations by a trial-and-error heuristic search in CGMD.

We first determine the length scaling factor: 1 mm in the experiment corresponds to 10 in the simulation. Taking the case of ρ = 50 mm and R = 5 mm in the experiment as an example, in the simulation, 500 was calculated to be the scaled radius of the substrate, and the scaled radius of the sheet was calculated to be 50. In the simulation, we selected the average distances of the discretized particles (the mesh size) in the sheet and substrate to be 2 and 1.5, respectively. The equilibrium distance σ between sheet particles was set to be 2, at which the potential energy between the sheet particles was zero, while the cutoff was set to be 2σ.

We then find an initial combination of the sheet bending rigidity, stretching stiffness, and adhesion energy as a starting point for our parameter calibration. The stretching coefficient (k_{s}) and bending coefficient (k_{bend}) were first calculated based on the Helfrich model. [47, 48] In the Helfrich model, $k_{\mathrm{s}} = \frac{Eh}{3^{0.5}(1-\nu^2)}$, and $k_{\mathrm{b}} = \frac{2Eh^3}{12\times 3^{0.5}(1-\nu^2)}$, where E is Young's modulus, h is thickness, and ν is the Poisson ratio. The potential well depth (ε) between substrate and sheet particles in the CGMD model governs the interfacial adhesion. To calculate the potential well depth, a sheet with a radius of 5 mm was placed at a distance σ above a square plate with a side length of 15 mm, as shown in **Fig. S7**. The adhesion energy was the total potential between the sheet particles and the substrate particles in the CGMD model. We then obtained an initial ε, and eventually, we found ε = 0.16 offered the adhesion energy per unit area of 0.144 J m^{-2}. Note that if the mesh size changes, the potential well depth must be recalibrated. However, this set of material properties was not the correct material parameters in simulation space since other units affected the unit conversion for the force unit. Therefore, it is essential to find the correct unit conversion for the forces.

After that, we performed a trial-and-error heuristic search to find the correct combination of k_{s}, k_{b}, and ε simultaneously employed them as material parameters. The correct property must achieve approximately the same sheet edge deflection, buckling number, and sheet conformability as the experiments. We performed this search based on two cases, sheets with radii of 5 mm and 7 mm on the substrate with a radius of 50 mm, as shown in **Fig. 3** and **Fig. S1.** The three macroscopic behaviors of both cases by CGMD simulation agreed well with their corresponding experimental results. Based on the physical parameter shown in Table S1, the calibrated stretching coefficient k_{s} and bending coefficient k_{bend} were 1500 and 4.313 for the lattice-spring model, respectively. The potential well depth (ε) between the substrates and the sheet particles is determined by adhesion energy per unit, as shown in **Fig. S8.** The equilibrium distance σ between the substrate and the sheet particle was set to be 0.2 mm. These calibrated parameters were used in all other cases. To demonstrate the validity of this combination of material parameters in simulation, the normalized maximum radius of complete contact $\bar{r} =$ c

$1.9(\gamma/Eh)^{1/4}$ can be calculated to be 0.068 in simulation and 0.070 in physical experiments. The error came from the adhesion energy calculation in simulation but is reasonably small.

In addition, the size scaling and top-down method will take two scaling factors: the length scaling factor, C_{length} and the force scaling factor, C_{force}. The length scaling factor can be written as $C_{\text{length}} = \frac{L_{\text{simulation}}}{L_{\text{physical}}} = 1 \times 10^4\ \text{m}^{-1}$, where $L_{\text{simulation}}$ and L_{physical} are the unit length in the simulation and physical space, respectively. The force scaling factor can be expressed as $C_{\text{force}} = \frac{F_{\text{simulation}}}{F_{\text{physical}}} = 5.88 \times 10^{-4}\ \text{N}^{-1}$, where $F_{\text{simulation}}$ and F_{physical} are the unit force in the simulation and physical space, respectively. Finally, based on the two scaling factors, the results from the simulation scale can be transformed into the experimental scale. In this work, we consider three types of substrate radii and a wide range of different sheet radii as listed in **Table S2**.

Table S2 Geometric parameters of substrate and sheet simulated by CGMD

Simulation		Physical (mm)		Sheet radius-to-substrate radius ratio
Substrate radius	Sheet radius	Substrate radius	Sheet radius	
300	30.0	30	3.0	0.10
	40.0		4.0	0.13
	50.0		5.0	0.17
	60.0		6.0	0.20
	70.0		7.0	0.23
	80.0		8.0	0.27
	90.0		9.0	0.30
	100.0		10.0	0.33
500	35.0	50	3.5	0.07
	50.0		5.0	0.10
	70.0		7.0	0.14
	100.0		10.0	0.20
	120.0		12.0	0.24
	140.0		14.0	0.28
700	35.0	70	3.5	0.05

	70.0		7.0	0.07
	90.0		9.0	0.10
	100.0		10.0	0.14
	120.0		12.0	0.17
	140.0		14.0	0.20

Besides, we studied the effect of the mesh size. In the above simulations, the distance of the discretized particles in the sheets (the mesh size) was selected to be 2 based on previous experiences. To study how the mesh size affects the sheet buckling, we took a sheet with a radius of 5 mm and a substrate with a radius of 50 mm as an example (Corresponding to a sheet with a radius of 50 and a substrate with a radius of 500 in simulations, and see simulation parameters in **Table S3** for details). We simulated the sheets conforming to the spherical substrates with four different mesh sizes, 0.5, 1, 2, and 4. We first calibrated the potential well depth ε and plotted it as a function of the mesh size, as shown in **Fig. S9A**. Then, five independent models were simulated for the same sheet and substrate radius. Their conformability is plotted in **Fig. S9B,** and their edge deflections are plotted in **Fig. S9C**. It can be observed that the mesh size does not play a significant role in these macroscopic buckling behaviors. Therefore, we choose 2.0 as the mesh size for all the following studies.

Table S3 The model parameters for the thin sheet with different mesh sizes

Mesh size	Particle number	Particle mass	Epsilon	Sigma	Cut off
0.5	32866	0.0258	0.010	2.0	4.0
1	8424	0.1007	0.028	2.0	4.0
2	2151	0.3945	0.085	2.0	4.0
4	610	1.3912	0.230	2.0	4.0

3. Computational Method for Cut-Facilitated Design

For cut-facilitated design, we first simulated the experiments using the above calibrated potential parameters to validate our simulation. Taking the sheet with a radius of 7 mm and the substrate with a radius of 50 mm as an example, we simulated l= 2 mm

and M = 3, l = 3 mm and M = 2, and l = 3 mm and M = 3 to compare their sheet conformability, contour plots of the gap between the sheet and the substrate, and the gap between the sheet and the substrate along the boundary of the circular sheet. In simulations, the sheet radius is 70 and the substrate radius is 500. The cut length l = 2 mm and 3 mm corresponds to l = 20 and 30, respectively.

After validation, to study how the cut-facilitated design affects the sheet conformability, we consider different cut lengths and cut numbers for a sheet with a radius of 10 mm on a substrate with a radius of 30 mm (Corresponding to a sheet with a radius of 100 and a substrate with a radius of 300 in simulations). **Table S4** lists the cut length and cut number we investigated by simulation. The mesh size of 2.0 is used in all CGMD simulations. Their conformability is calculated and plotted in **Fig. 6C.**

Table S4 Different combinations of cut length and cut number

The substrate with a radius of 300 and the thin sheet with a radius of 100						
Cut length l	Cut number M					
10	2	3	4	6	8	10
30	2	3	4	6	8	10
50	2	3	4	6	8	10
70	2	3	4	6	8	10
90	2	3	4	6	8	10

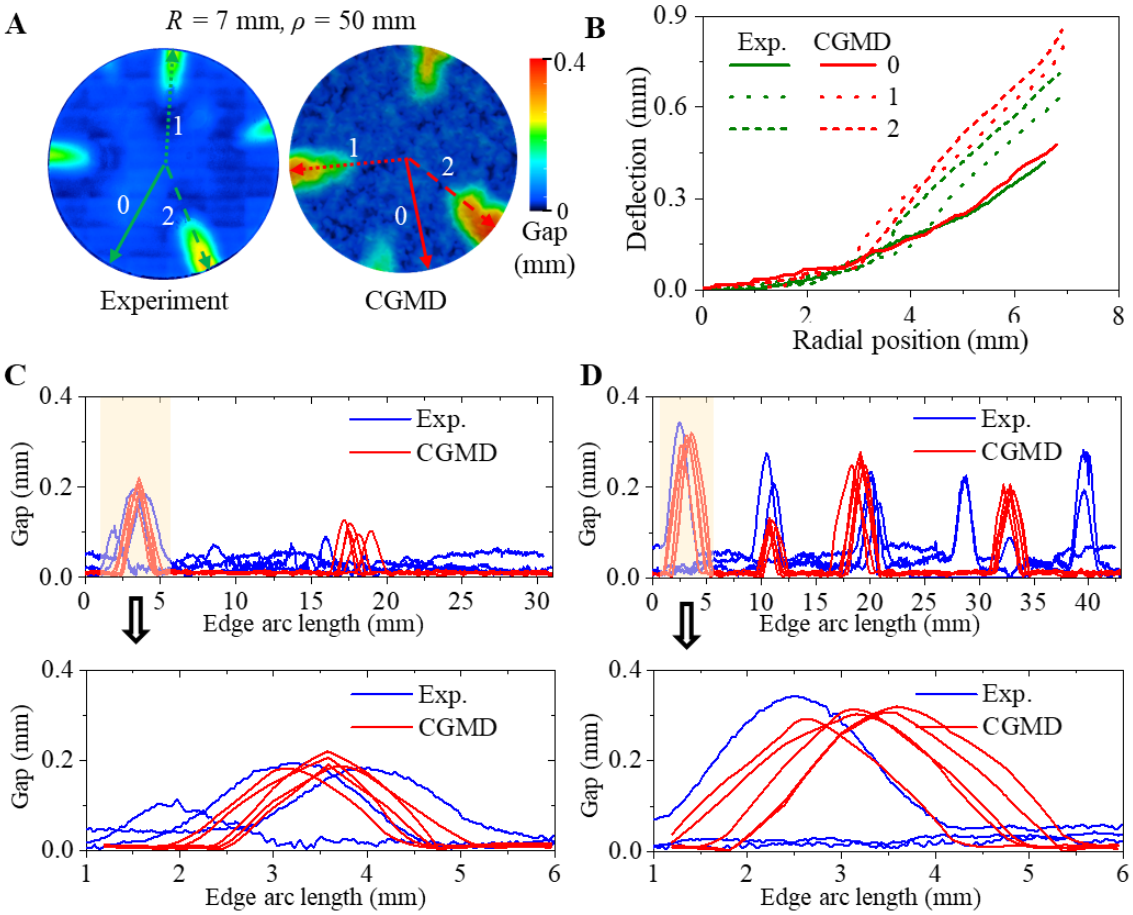

Figure S1. The gap between the sheet and substrate obtained by experiment and CGMD. (**A**) Contour plots of the gap between the sheet and the substrate by optical 3D scan (left) and CGMD simulation (right) for the case of R = 7 mm and ρ = 50 mm. (**B**) Corresponding sheet deflection along the radial direction at fully conformed region (solid curves) and the axes of symmetry of two buckles (dashed and dotted curves). The gap between the sheet and the substrate along the edge of the sheet of five optical 3D scan experiments (blue) and five independent CGMD simulations (red) for the cases of (**C**) R = 5 mm and ρ = 50 mm and (**D**) R = 7 mm and ρ = 50 mm. The zoomed-in profiles of the first blister are shown at the bottom.

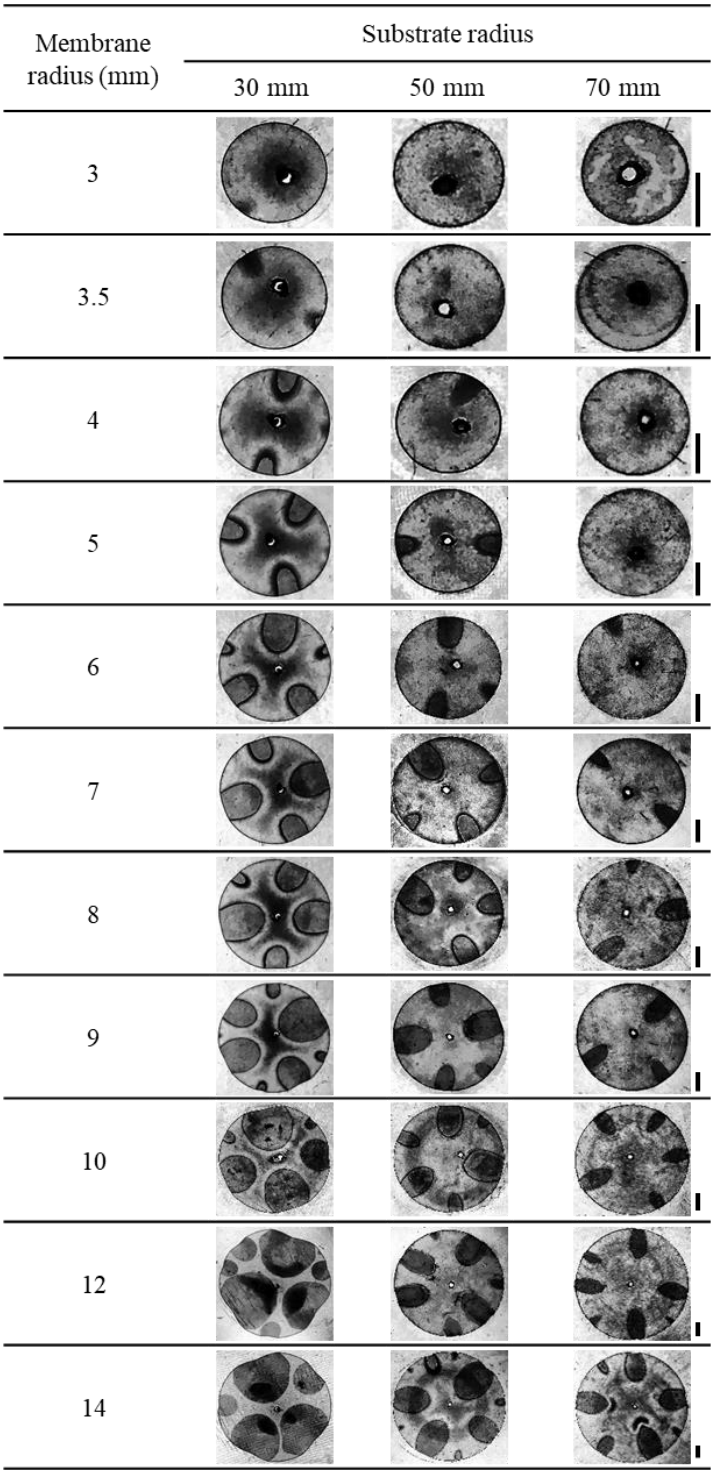

Figure S2. Greyscale images of top-down optical micrographs for different sheet radii and different substrate radii. The scale bars denote 3 mm.

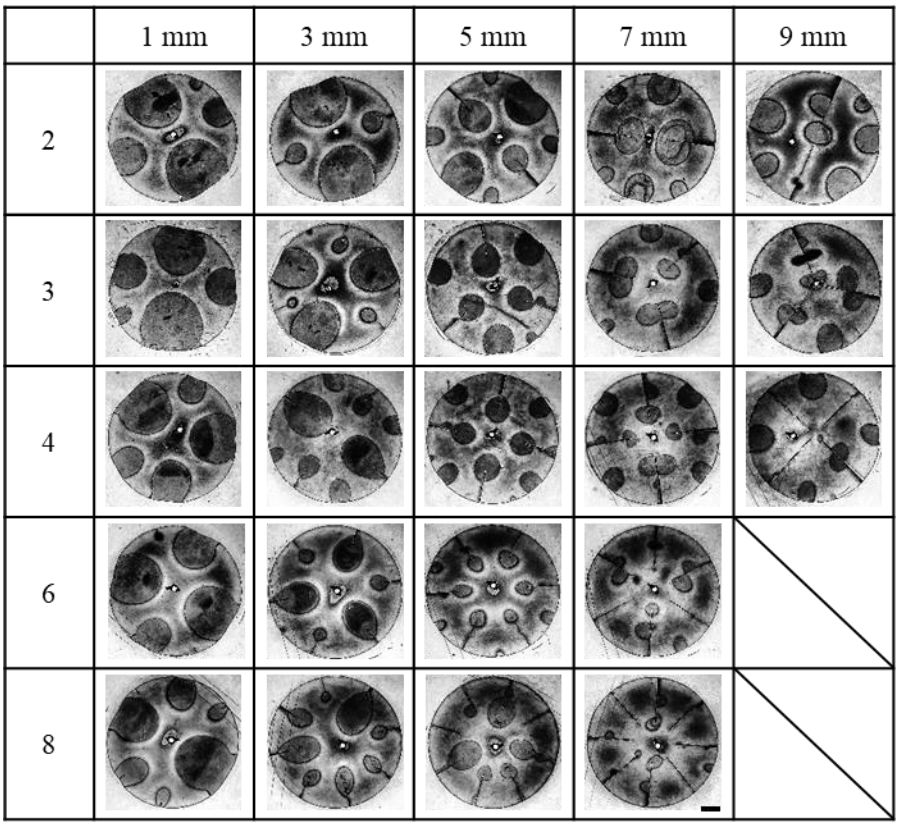

Figure S3. Greyscale images of top-down optical micrographs for different cut lengths and different cut numbers for the case R = 10 mm, ρ = 30 mm. The scale bar denotes 3 mm.

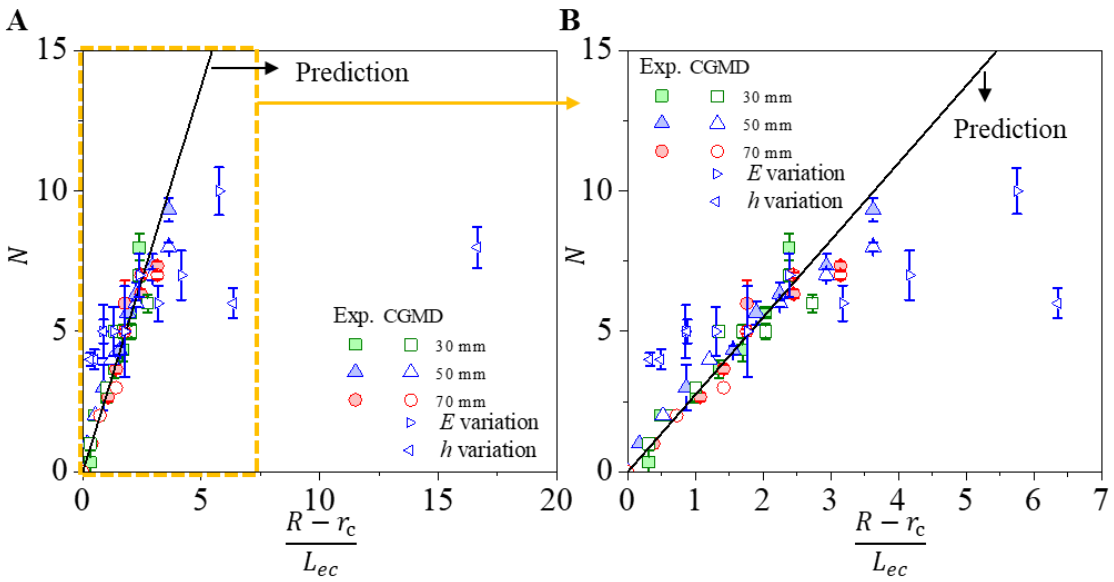

Figure S4. Buckle number for thin sheets with different moduli and thicknesses. (A) Buckle number in experiments (hollow markers), simulations (filled markers), and prediction by Eq. (11) with fitted coefficient based on 3 GPa and 13-μm-thick sheets (solid line). Green, blue, and red denote the substrate radius of 30 mm, 50 mm, and 70 mm, respectively. The triangular markers with a corner pointing to the left denotes simulations with various modulus E and fixed thickness h. The triangular markers with a corner pointing to the right denotes simulations with various thickness h and fixed modulus E. **(B)** An zoom-in view when $(R - r_c) / L_{ec}$ is small.

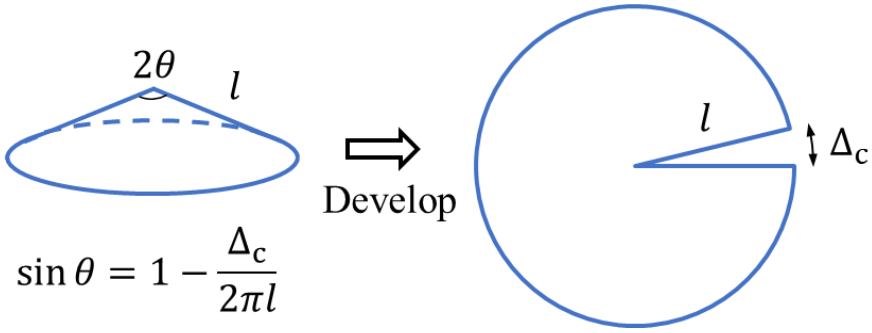

Figure S5. The schematic of a 3D cone developed into a planar circle with a wedge opening.

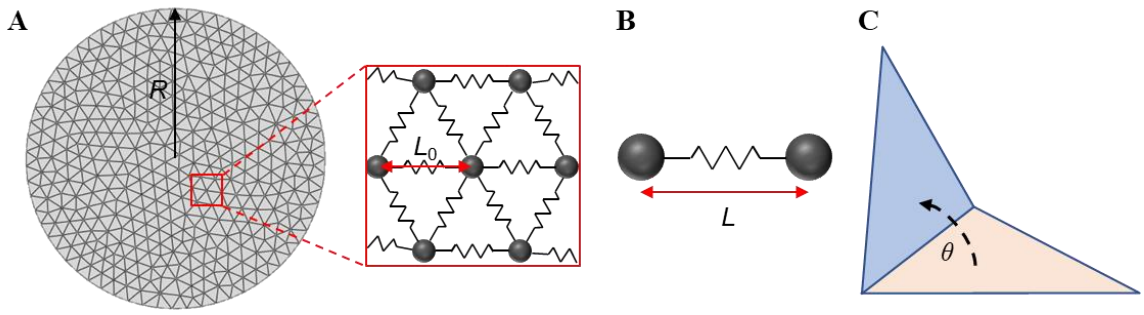

Figure S6. A CGMD model for the thin sheet. (**A**) A circular elastic sheet was discretized into a triangulated network, where particles with mass were located at the lattice points with bonds and elements defined. (**B**) Stretching energy was defined for each bond based on Hooke's Law with an initial bond length of L_0. (**C**) Bending energy was defined for each pair of neighbor elements based on the dihedral angle θ.

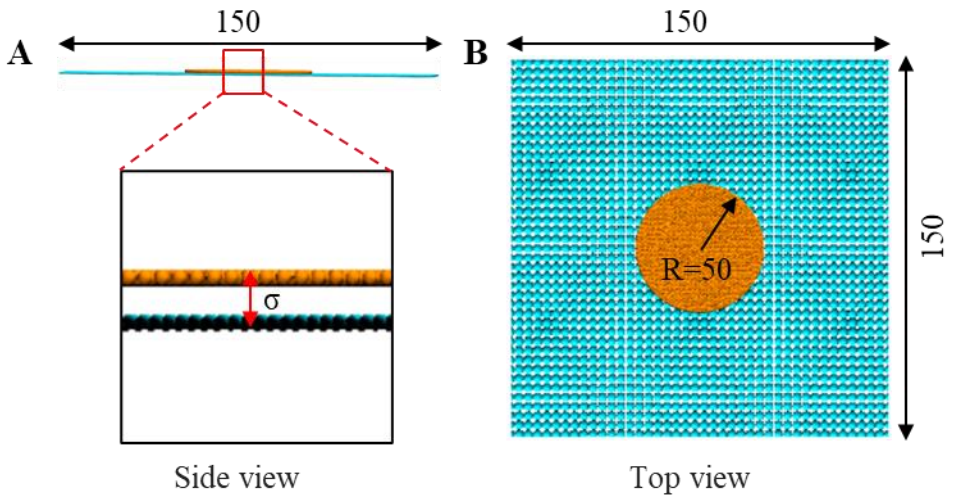

Figure S7. Calibration of interfacial adhesion for the CGMD model. (**A**) side view and (**B**) top view of a 5-mm-radius circular sheet placed on a flat substrate with a distance of σ.

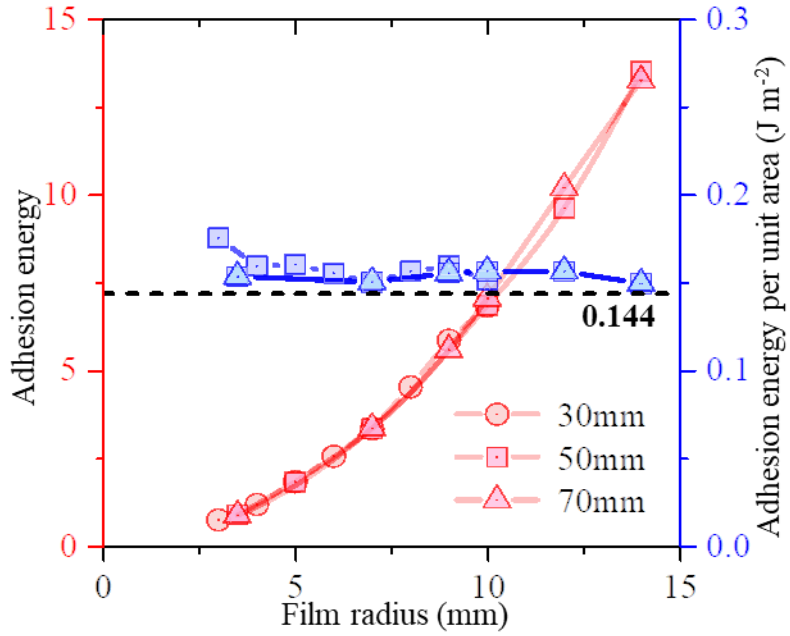

Figure S8. Investigation of adhesion energy for different *R* and *ρ*. The calculated adhesion energy per unit area dominates the well depth of L-J potential for different sheet radii and substrates. The black dashed line defines the adhesion energy in experiments. The red color represents the total adhesion energy between substrate and sheet in simulations. The blue color shows the adhesion energy per unit area between substrate and sheet in simulations, which all are close to the experimental value (0.144 J m^{-2}).

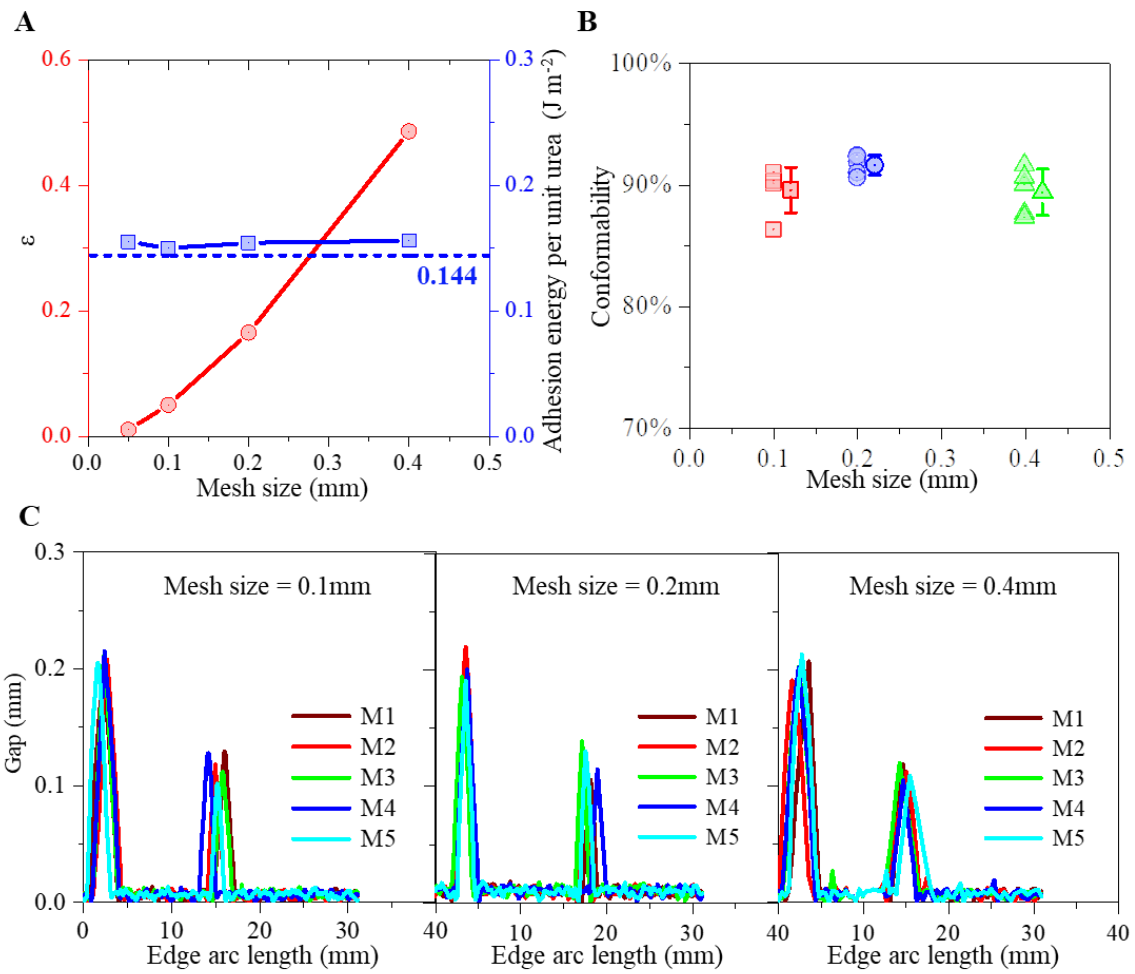

Figure S9. Investigation of proper mesh size in the exemplary case of R = 5 mm and ρ = 50 mm. (**A**) Calibrated well depth of L-J potential and adhesive energy per unit area for different mesh sizes. (**B**) Sheet conformability with different mesh sizes. (**C**) The gap between the sheet and the substrate along the circle boundary for different mesh sizes. Five independent simulations are performed for each case (M1-M5).

Supplementary Movies:

Movie S1. The top-down view of the conforming process of a thin sheet of R = 7 mm, h = 13 μm and E = 3 GPa on a spherical substrate of ρ = 50 mm in CGMD simulation.

Movie S2. The top-down view of the conforming process of a thin sheet of R = 9 mm, h = 52 μm and E = 3 GPa on a spherical substrate of R = 9 mm and ρ = 30 mm in CGMD simulation.

Movie S3. The top-down view of the conforming process of a thin sheet of R = 15 mm, h = 13 μm and E = 3 GPa with 12 curved cuts of 12.9 mm long on a spherical substrate of R = 9 mm and ρ = 30 mm in CGMD simulation.